CANCER

Metabolic traits shape responses to LSD1-directed therapy in glioblastoma tumor-initiating cells

Giulia Marotta[1], Daniela Osti[1], Elena Zaccheroni[1], Brunella Costanza[1], Stefania Faletti[1,2], Adriana Marinaro[1], Cristina Richichi[1], Deborah Mesa[1], Simona Rodighiero[1], Chiara Soriani[1], Enrica Migliaccio[1], Federica Ruscitto[1], Chiara Priami[1], Sara Sigismund[1,3], Francesco Manetti[4], Dario Polli[4,5], Galina V. Beznusenko[6], Mara-Camelia Rusu[7], Francesco Favero[8], Davide Corà[8], Domenico A. Silvestris[9], Angela Gallo[9], Valentina Gambino[1], Fabio Alfieri[1], Sara Gandini[1], Matthias J. Schmitt[7], Gaetano Gargiulo[7], Roberta Noberini[1], Tiziana Bonaldi[1,3], Giuliana Pelicci[1,10]*

Lysine-specific histone demethylase 1A (LSD1) is an epigenetic regulator involved in various biological processes, including metabolic pathways. We demonstrated the therapeutic potential of its pharmacological inhibition in glioblastoma using DDP_38003 (LSD1i), which selectively targets tumor-initiating cells (TICs) by hampering their adaptability to stress. Through biological, metabolic, and omic approaches, we now show that LSD1i acts as an endoplasmic reticulum (ER) stressor, activating the integrated stress response and altering mitochondrial structure and function. These effects impair TICs' oxidative metabolism and generate reactive oxygen species, further amplifying cellular stress. LSD1i also impairs TICs' glycolytic activity, causing their metabolic decline. TICs with enhanced glycolysis benefit from LSD1-directed therapy. Conversely, metabolically silent TICs mantain ER and mitochondrial homeostasis, adapting to stress conditions, including LSD1i treatment. A dropout short hairpin RNA screening identifies postglycosylphosphatidylinositol attachment to proteins inositol deacylase 1 (PGAP1) as a mediator of resistance to LSD1i. Disruptions in ER and mitochondrial balance holds promise for improving LSD1-targeted therapy efficacy and overcoming treatment resistance.

INTRODUCTION

Glioblastoma (grade 4 glioma; GBM) is a highly aggressive and heterogeneous tumor of the central nervous system, posing a serious challenge for both patients and health care systems (*1*). Despite decades of research advancements and evolving clinical practices, GBM remains incurable. The current standard of care, consisting of surgery followed by chemoradiotherapy with temozolomide (TMZ), has only modest improved survival rates and time to relapse (*2*).

GBM aggressiveness is driven by extensive intertumoral and intratumoral heterogeneity, with distinct molecular and cellular phenotypes continuously evolving in response to treatment. In this complex context, tumor-initiating cells (TICs) within each tumor have been identified as key drivers of GBM onset and growth, treatment resistance, and intratumoral heterogeneity (*3*). Single-cell approaches highlighted that each tumor is a composite system in which the conversion between TICs and non-TICs is dynamic and TICs themselves are in continuous evolution (*4*). TICs shift between different cellular states, each with distinct molecular profiles and functional properties that vary spatially and temporally within individual tumors. Their plasticity is closely linked to their metabolic behaviors, which dictate their adaptation to contextual microenvironmental stresses and drug cues, allowing their survival under energetically unfavorable conditions (*5*–*8*).

Recent studies highlighted the metabolic heterogeneity of GBM TICs, with different GBM subtypes showing distinct metabolic preferences (*9*). Some TICs manifest a quiescent, slow-cycling phenotype characterized by lower glycolytic activity, reduced extracellular acidification rate, and decreased oxygen consumption (*10*). TICs defined as proneural rely on glycolysis, recalling the Warburg effect observed in bulk GBM cells (*11*), while mesenchymal TICs can switch between glycolysis and oxidative phosphorylation (OXPHOS), depending on microenvironmental signals and metabolic demands (*12*). They can exploit alternative nutrient resources such as glutamine (*13*), fatty acid (*14*), and fructose (*15*), demonstrating remarkable metabolic flexibility.

In GBM, the interplay between metabolism and epigenetics contributes to metabolic rewiring and alterations in histone/DNA modifications (*16*) that ultimately affect the molecular classification of the tumor. As a consequence, the targeting of epigenetic regulators is widely investigated in clinical trials (*17*–*19*). We have recently demonstrated that the pharmacological inhibition of lysine-specific histone demethylase 1A (LSD1) with the selective LSD1 inhibitor DDP_38003 (hereafter LSD1i) (*20*) synergizes with various stressors to trigger a maladaptive integrated stress response (ISR), leading to the death of stressed TICs, thus highlighting LSD1 as a relevant therapeutic target in human GBM (*21*). In addition, LSD1 affects diverse metabolic processes such as glycolysis, mitochondrial function, and lipid metabolism in different cellular contexts (*22*–*27*).

[1]Department of Experimental Oncology, European Institute of Oncology (IEO), IRCCS, Milan 20139, Italy. [2]Human Technopole, Viale Rita Levi-Montalcini, 1, Milan 20157, Italy. [3]Department of Oncology and Hematology-Oncology, Università degli Studi di Milano, Milan Italy. [4]Department of Physics, Politecnico di Milano, Milan, Italy. [5]CNR Institute for Photonics and Nanotechnology (CNR-IFN), Milan, Italy. [6]IFOM ETS–The AIRC Institute of Molecular Oncology, Milan, Italy. [7]Max-Delbrück-Center for Molecular Medicine (MDC) in the Helmholtz Association, Berlin, Germany. [8]Department of Translational Medicine, Center for Translational Research on Autoimmune and Allergic Disease (CAAD), University of Piemonte Orientale, Novara 28100, Italy. [9]Unit of Genetics and Epigenetic of Pediatric Cancer, Oncohaematology Department, IRCCS Ospedale Pediatrico Bambino Gesù, Viale di San Paolo 15, Rome 00146, Italy. [10]Department of Translational Medicine, University of Piemonte Orientale, Novara 28100, Italy.
*Corresponding author. Email: giuliana.pelicci@ieo.it

In this study, we demonstrate that LSD1i functions itself as an endoplasmic reticulum (ER)–stress agent, which induces perturbations of calcium (Ca^{2+}) homeostasis and redox imbalance, and prompts structural and functional dysfunctions in mitochondria that affect TIC metabolism. LSD1i-directed therapy is only effective in a subset of GBM TICs, specifically those with elevated glycolytic activity. LSD1i-resistant TICs, which exhibit a silent metabolic phenotype (*28*), are also less susceptible to the metabolic and stress challenges posed by known ER stressors such as thapsigargin (Tg) and tunicamycin (TU). They can preserve mitochondria and ER homeostasis, which likely enables them to adapt to changes of the tumor microenvironment. Consequently, both the pivotal role of LSD1 in orchestrating energy flow and metabolic adaptation in GBM TICs, along with the various metabolic characteristics of GBM TICs that are associated with either therapeutic response or resistance to LSD1i, lay the foundation for identifying metabolic pathways as suitable candidate targets for therapeutic intervention.

RESULTS

LSD1i treatment induces ISR and mitochondrial perturbations in GBM TICs

We previously demonstrated that LSD1 is a crucial regulator of GBM TIC survival, adaptation, and recovery from stress, and its pharmacological inhibition via the irreversible molecule LSD1i (*20*) hampers the activation of the ISR, which leads to the death of TICs exposed to ER stress or nutrient deficiency (*21*). Here, we provide evidence that LSD1i triggers the ISR by itself. Western blot analysis of activating transcription factor 4 (ATF4), the master regulator of the ISR (*29*), revealed its accumulation in GBM TICs isolated from different patients (GBM#22 and GBM#7) exposed to LSD1i (Fig. 1A). Notably, ATF4 induction occurred independently of phosphorylation of eIF2α (Fig. 1A). Accordingly, in LSD1i-treated TICs from different patients with GBM (GBM#22, GBM#7, GBM#10, and GBM#18), we measured increased formation of stress granules—cytosolic membraneless bodies accumulating in the cytoplasm as a direct outcome of ISR induction (Fig. 1B and fig. S1A) (*30*). G3BP1 and its paralogs are members of Ras–guanosine triphosphatase–activating protein (Src homology 3 domain)–binding proteins and are known to take part in stress granule assembly upon activation of stress response programs such as the ISR.

A substantial body of literature emphasizes the link between the induction of ISR and mitochondrial dysfunction, as well as the specific activation of ATF4 signaling through the ISR in response to mitochondrial stress (*31*–*34*). Building on these notions and considering the ability of LSD1i to induce an ISR (Fig. 1, A and B), we investigated whether LSD1i treatment could affect the physiology of TIC mitochondria. While vehicle-treated GBM TICs exhibited mitochondria with a tubular and network-like shape, which is typical of healthy organelles, mitochondria in LSD1i-treated cells significantly lost the branched organization, acquiring a round shape (Fig. 1C and fig. S1B). The remodeling of mitochondrial network was associated with effects on several mitochondrial parameters. We measured a hyperpolarized mitochondrial membrane potential ($\Delta\Psi m$) (Fig. 1D and fig. S1C) and a significant increase in the mitochondrial redox ratio (Fig. 1E and fig. S1D) upon LSD1i treatment, with no concurrent alteration in mitochondrial mass (Fig. 1F and fig. S1E). Notably, these are recognized as signs of distress, often interconnected and occurring in apoptotic cells (*35*–*38*), and are associated with compromised mitochondrial functionality (*39*–*41*). A detailed examination of mitochondrial respiration revealed a significant reduction in both basal and maximal levels of the oxygen consumption rate (OCR) in LSD1i-treated GBM TICs, along with a decrease in spare respiratory capacity. Nonmitochondrial respiration showed no significant changes (Fig. 1G and fig. S1F). LSD1i treatment also affected the glycolytic activity with GBM TICs exhibiting a decreased basal and compensatory glycolysis, as indicated by measurements from the glycolytic rate assay (Fig. 1H and fig. S1G) and the extracellular acidification rate (ECAR) determined using the mitostress test (fig. S1, H and I). The bioenergetic profile graph demonstrated that treated TICs were unable to enhance glycolysis efficiently to compensate for mitochondrial damage induced by LSD1i (Fig. 1I). This led to a decline in adenosine 5′-triphosphate (ATP) production from both OXPHOS and glycolysis (Fig. 1J and fig. S1J). Consistent with these data, gene set enrichment analysis (GSEA) based on transcriptional changes induced by LSD1i treatment and genes associated with mitochondrial pathways from MitoCarta database (*42*) revealed a global reduction in categories related to mitochondrial structure and trafficking, as well as the metabolism of energy-related products (carbohydrate, nucleotide, and amino acids) (Fig. 1K).

Overall, these results reveal that LSD1i induces mitochondrial dysfunctions disrupting energy pathways (both glycolysis and mitochondrial respiration), which ultimately leads to the death of GBM TICs, as previously described (*21*). This aligns with the notable association between LSD1 expression and genes related to glycolysis and OXPHOS in GBM samples from two independent cohorts, the Chinese Glioma Genome Atlas (CGGA) and Gravendeel dataset (Fig. 1L) (*43*), and reflects LSD1's role in regulating various metabolic processes, including glycolysis and mitochondrial function (*22*, *25*).

LSD1i increases functional ER-mitochondrial coupling

Stress conditions such as ER stress, nutrient deprivation, oxidative stress, or metabolic dysregulation can disrupt the physical communication and function between mitochondria and the ER, leading to metabolic dysfunction (*44*, *45*). In line with these observations, treating GBM TICs with Tg, a known ER stress inducer (*46*), caused mitochondria to become rounded in shape (fig. S2A), increased their membrane potential (fig. S2B), and enhanced their physical contacts with ER, as indicated by the extent of the length covered by mitochondria-ER contact sites (MERCs) (fig. S2C). Similarly, electron microscopy (EM) analysis of LSD1i-treated TICs revealed a significant increase in MERC length (Fig. 2A). This increased physical coupling significantly altered intracellular Ca^{2+} homeostasis (Fig. 2B) and increased the levels of both mitofusin 1 (MFN1) and MFN2, key proteins that mediate mitochondrial morphology and link the ER and mitochondria (Fig. 2C). Together, these data indicate that stress signals originating from LSD1i mirror those caused by Tg (fig. S2D), compromising mitochondrial function (Fig. 1).

Interpatient heterogeneity reveals TICs resistant to LSD1i treatment

LSD1i has broad therapeutic potential for treating GBM TICs with diverse molecular profiles (*21*). One of the major challenges in developing effective therapeutic interventions is the heterogeneity in treatment responses observed in GBMs (*8*). LSD1i has a median effective concentration (EC_{50}) value of 2.5 μM in GBM TICs (*21*), which aligns with its specificity for LSD1 (*20*). By transplanting

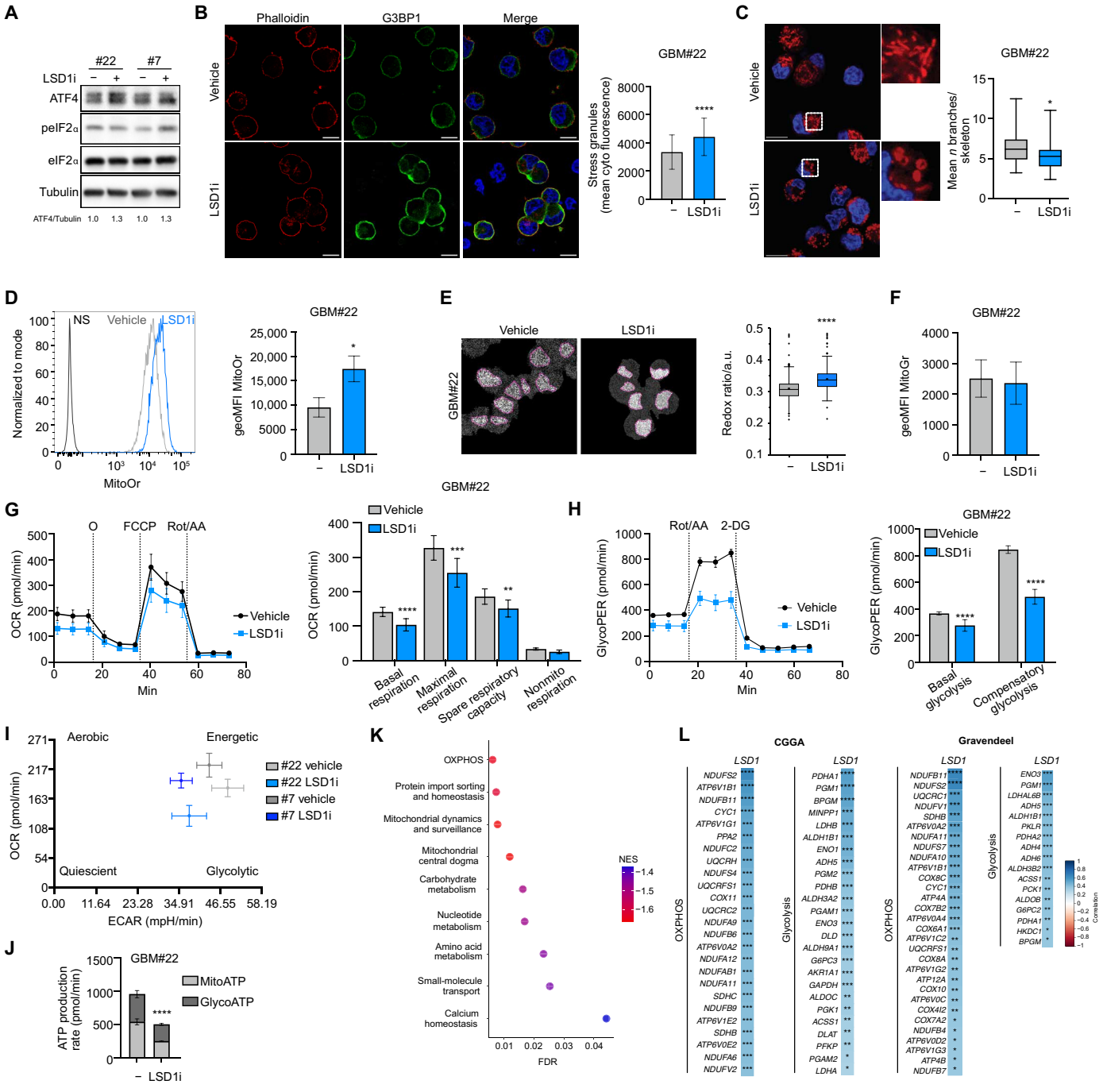

Fig. 1. LSD1i treatment induces ISR and mitochondrial perturbations in GBM TICs. (**A**) Representative immunoblot of ATF4, peIF2a, eiF2α and tubulin after LSD1i, normalized to untreated TICs ($n = 3$). (**B**) Representative images (left) and quantification (right) of G3BP1 stress granules (green), actin (red), and DNA (blue). Scale bars, 10 μm (vehicle, $n = 4509$ cells; LSD1i, $n = 2916$ cells; means ± SD). (**C**) Representative images of mitochondrial structure (left). Enlarged highlighted areas (dashed boxes) are shown. Mitochondrial fragmentation quantification (right). Scale bars, 10 μm. ($n = 3$; means ± SD). (**D**) Representative histograms (left) and quantification (right) of ΔΨm (MitoOr, mitotracker orange) ($n = 7$; means ± SEM). NS, not stained; geoMFI, geometric mean fluorescence intensity. (**E**) Representative images (left) and quantification (right) of redox ratio (vehicle, $n = 155$ cells; LSD1i, $n = 297$ cells; means ± SD). a.u., arbitrary units. (**F**) Mitochondrial mass quantification (MitoGr, mitotracker green) ($n = 5$; means ± SEM). (**G**) OCR kinetic graph (left); addition of oligomycin (O), carbonyl cyanide *p*-trifluoromethoxyphenylhydrazone (FCCP), and rotenone plus antimycin A (Rot/AA) is indicated. Respiration parameter quantification (right) ($n = 3$; means ± SD). (**H**) Glycolytic proton efflux rate (glycoPER) kinetic graph (left); addition of Rot/AA and 2-deoxyglucose (2-DG) is indicated. Basal and compensatory glycolysis quantification (right) ($n = 3$; means ± SD). (**I**) Energy map plotting OCR and ECAR obtained in (G) and fig. S1H. (**J**) Mitochondrial ATP (mitoATP) and glycolytic ATP (glycoATP) production rate ($n = 3$ replicates per group; means ± SD). (**K**) GSEA analysis of mitochondrial pathways post-LSD1i treatment. (**L**) Heatmap correlating LSD1 with OXPHOS and glycolysis genes in GBM datasets. Top 25 correlated genes of the OXPHOS signature are shown. $^{****}P_{adj} = 0$; $^{***}P_{adj} < 0.001$; $^{**}P_{adj} < 0.01$; $^{*}P_{adj} < 0.05$. Two-tailed unpaired Student's *t* test, $^{*}P < 0.05$; $^{**}P < 0.01$; $^{***}P < 0.001$; $^{****}P < 0.0001$ for (D), (F) to (H), and (J). Mann-Whitney *U* test, $^{*}P < 0.05$; $^{****}P < 0.0001$ for (B), (C), and (E).

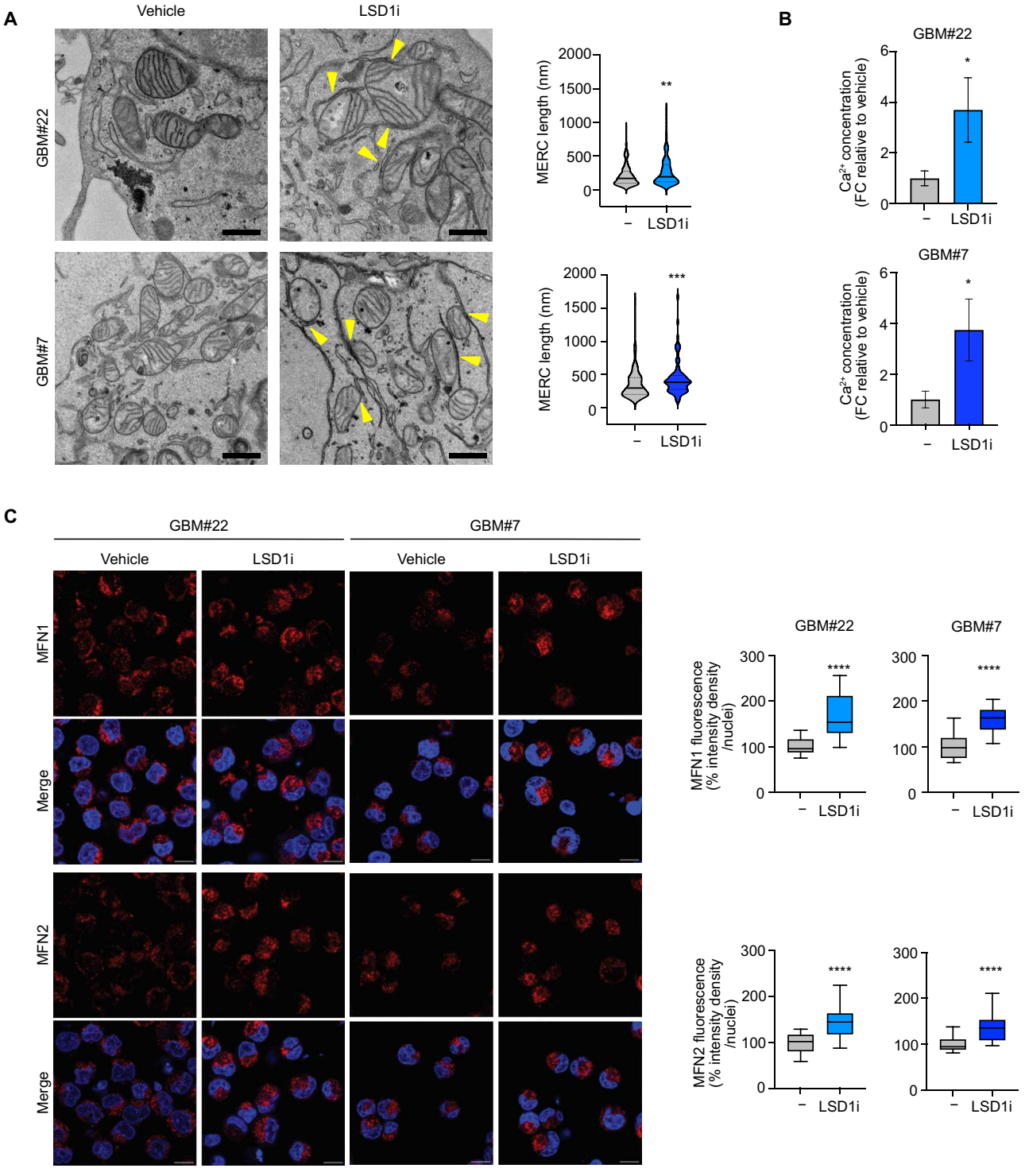

Fig. 2. LSD1i increases functional ER-mitochondrial coupling. (**A**) Representative transmission EM (TEM) images of mitochondria and ER in GBM#22 and GBM#7 TICs after LSD1i. Yellow arrowheads indicate MERCs. Scale bars, 500 nm ($n = 20$ cells for each condition; means ± SD). The quantification of MERC length with and without LSD1i treatment is shown. (**B**) Measurements of Ca^{2+} concentration by Rhod-2 fluorescence signal quantification in GBM#22 and GBM#7 TICs following LSD1i treatment ($n = 3$; means ± SD). (**C**) Representative confocal images (left) and quantification (right) of MFN1 and MFN2 (red) in GBM#22 and GBM#7 TICs after LSD1i treatment, with 4′,6-diamidino-2-phenylindole (DAPI) (blue) as a nuclear stain. Cell counts for each condition: GBM#22 ($n = 3$; means ± SD). Two-tailed unpaired Student's *t* test, $^{*}P < 0.05$ for (B); Mann-Whitney *U* test, $^{**}P < 0.01$; $^{***}P < 0.001$; $^{****}P < 0.0001$ for (A) and (C).

LSD1i-treated GBM TICs into zebrafish larvae, a powerful model for assessing drug sensitivity and in vivo outcomes (*47*), we demonstrated that, in addition to samples sensitive to LSD1i-directed therapy (hereafter referred to as LSD1i^{Sens} TICs), a subset of patient-derived TICs displayed resistance to LSD1i (referred to as LSD1i^{Res} TICs). LSD1i treatment of LSD1i^{Sens} TICs resulted in significantly smaller tumors in zebrafish xenografts (Fig. 3A), while treatment of LSD1^{Res} TICs did not affect tumor volume, even at higher LSD1i concentrations (Fig. 3B). In line with these results, we previously demonstrated that LSD1i-directed therapy reduced tumor growth in mouse patient-derived xenografts (PDXs) from samples now categorized as LSD1i^{Sens} TICs (*21*). LSD1i exerted no effect on mouse PDXs transplanted with LSD1i^{Res} TICs, as no differences were observed in tumor growth (Fig. 3C) and mouse survival (Fig. 3D) in the representative LSD1i^{Res} GBM#23 PDX. Notably, LSD1i administration markedly increased the levels of H3K4me1 and H3K4me2 histone marks in the brains of GBM PDXs demonstrating its on-target effect (Fig. 3E). The immunocompetent GL261 GBM model (*48*) was also resistant to LSD1i treatment: Tumors grew to a similar extent in both control and LSD1i-treated mice without a survival benefit (fig. S3A).

On the basis of the responses in the two xenograft models, we further assessed the cellular phenotypes of LSD1i^{Res} TICs in vitro. We observed no changes in proliferation, even upon prolonged exposure to increasing doses of LSD1i (Fig. 3F and fig. S3B), cell death (Fig. 3G and fig. S3C), and self-renewal (Fig. 3H and fig. S3D). Among doses higher than the EC_{50} and beyond the compound's specificity range (*20*), only 10 μM inhibited TIC growth. Accordingly, TICs resistant to LSD1i maintained healthy and functional mitochondria upon LSD1i treatment. We measured no alterations in mitochondrial structure (Fig. 3I and fig. S3E), membrane potential (Fig. 3J and fig. S3F), and redox status (Fig. 3K and fig. S3G) in LSD1i-treated cells, the latter indicating the lack of significant reactive oxygen species (ROS) changes in these samples. Similarly, there were no changes in MERCs (Fig. 3L and fig. S3H) and Ca^{2+} concentrations (Fig. 3M and fig. S3I).

Resistance to LSD1-directed therapy occurred in TIC from various patients with GBM regardless of their genetic alteration status (table S1). Notably, the effects of *LSD1* genetic silencing in LSD1i^{Res} TICs extended beyond those of LSD1 pharmacological targeting, resulting in significant impairment in TIC growth (fig. S3J) and self-renewal (fig. S3K), and a pronounced reduction in tumor size in zebrafish xenografts (fig. S3L).

LSD1i^{Sens} and LSD1i^{Res} TICs display different metabolic features

To gain insights into the molecular mechanisms underlying the sensitivity or resistance to LSD1i and having excluded gene/pathway mutation peculiarities as determinants of LSD1i response (*21*) (table S1), we next compared the transcriptomic (Fig. 4A) and proteomic (Fig. 4B) profiles from a panel of LSD1i^{Sens} TICs ($n = 5$) and LSD1i^{Res} TICs ($n = 5$). Compared to LSD1i^{Res} TICs, LSD1i^{Sens} TICs exhibited a significant enrichment in stress-related signatures (Fig. 4, A and B), including unfolded protein response (UPR), hypoxia and ROS signaling, heat shock, and the heat stress responses, as well as the activation of type I interferons, tumor necrosis factor–α (TNF-α), transforming growth factor–β (TGF-β), and the nuclear factor κB (NF-κB) pathways, and apoptosis (Fig. 4A). Notably, the specific expression of these different pathways aligns with the aforementioned results reporting the major susceptibility of LSD1i^{Sens} TICs to perceive the stress imposed by LSD1i or by Tg. LSD1i^{Sens} TICs were also sustained by glycolysis and OXPHOS (Fig. 4A). Likewise, the activation of proliferation-related pathways (E2F and MYC) and mechanistic target of rapamycin complex 1 (MTORC1) pathway in samples sensitive to LSD1i well associates with their high rate of glycolysis, as indicated also in other cancer types (*49*, *50*). Notably, resistant TICs showed no enrichment in either stress response pathways or metabolic pathways, underscoring the differences in the metabolic phenotypes of these samples (fig. S4, A and B). We next assessed glycolysis and respiratory function in representative LSD1i^{Sens} TICs (GBM#22 and GBM#7) and LSD1i^{Res} TICs (GBM#23 and GBM#25) using Seahorse flux analyzer. LSD1i^{Sens} TICs exhibited increased glycolysis compared to LSD1i^{Res} TICs, both at the basal state and after the injection of mitochondrial inhibitors (Fig. 4C and fig. S4C). We did not find any difference in basal, maximal OCR, spare respiratory capacity, ATP production, and nonmitochondrial respiration among sensitive and resistant samples (fig. S4D). In accordance with the increased glycolytic activity, LSD1i^{Sens} TICs had a higher glucose uptake capacity (Fig. 4D) and notable increased expression of key glycolytic enzymes, including hexokinases (HKI and HKII), pyruvate kinase isozyme M2 (PKM2), phosphofructokinase platelet (PFKP), glyceraldehyde-3-phosphate dehydrogenase (GAPDH), and lactate dehydrogenase A (LDHA) (Fig. 4E). Hexokinase, which performs a key irreversible step in glycolysis, demonstrated a higher activity in sensitive samples (Fig. 4F). To further validate the differential reliance on glycolysis, we cultured TICs under different glucose concentrations. LSD1i^{Sens} TICs displayed reduced growth in both low-glucose (1 g/liter) and glucose-free media (Fig. 4G). In contrast, the growth of LSD1i^{Res} TICs was diminished only by glucose withdrawal and to a lesser extent than that of LSD1i^{Sens} cells (Fig. 4G). Similarly, LSD1i^{Sens} TICs were more sensitive to inhibition of glycolysis using 2-deoxyglucose (2-DG), an inhibitor of hexokinase (*51*), than resistant ones (Fig. 4H).

Collectively, these findings underline the existence of different metabolic phenotypes and adaptive responses between LSD1i^{Sens} and LSD1i^{Res} TICs. LSD1i^{Sens} TICs display enhanced glycolytic activity and increased expression of glycolysis-related genes. In contrast, LSD1i^{Res} TICs show lower glycolytic activity compared to LSD1i^{Sens} cells but have a similar OCR, without evidence for other specifically activated metabolic pathways indicative of a silent metabolic phenotype (*28*). They retain mitochondrial dynamics and function, likely suggesting a greater dependence on mitochondrial function. Consistent with this, the comparison between the transcriptomic profiles of samples resistant to LSD1i and the metabolism-associated GBM subtypes (*5*) revealed that LSD1i-resistant cells are associated with the mitochondrial subtype of GBMs (fig. S4E). This enables LSD1i^{Res} TICs to preserve their growth under conditions that are challenging for LSD1i^{Sens} cells, including LSD1i treatment, glucose deprivation, and inhibition of glycolysis.

LSD1i^{Res} TICs maintain mitochondrial integrity to better cope with ER stress

We previously demonstrated that Tg treatment alters mitochondrial structure and function in LSD1i^{Sens} TICs similarly to LSD1i, suggesting a shared cellular response among these stressors. On the basis of these results, we measured the downstream consequences of ER stress exposure in LSD1i^{Res} TICs to assess their ability to handle stressful cues other than LSD1i. Both mitochondrial morphology (Fig. 5A) and $\Delta\Psi m$ (Fig. 5B) were retained in LSD1i^{Res} TICs under

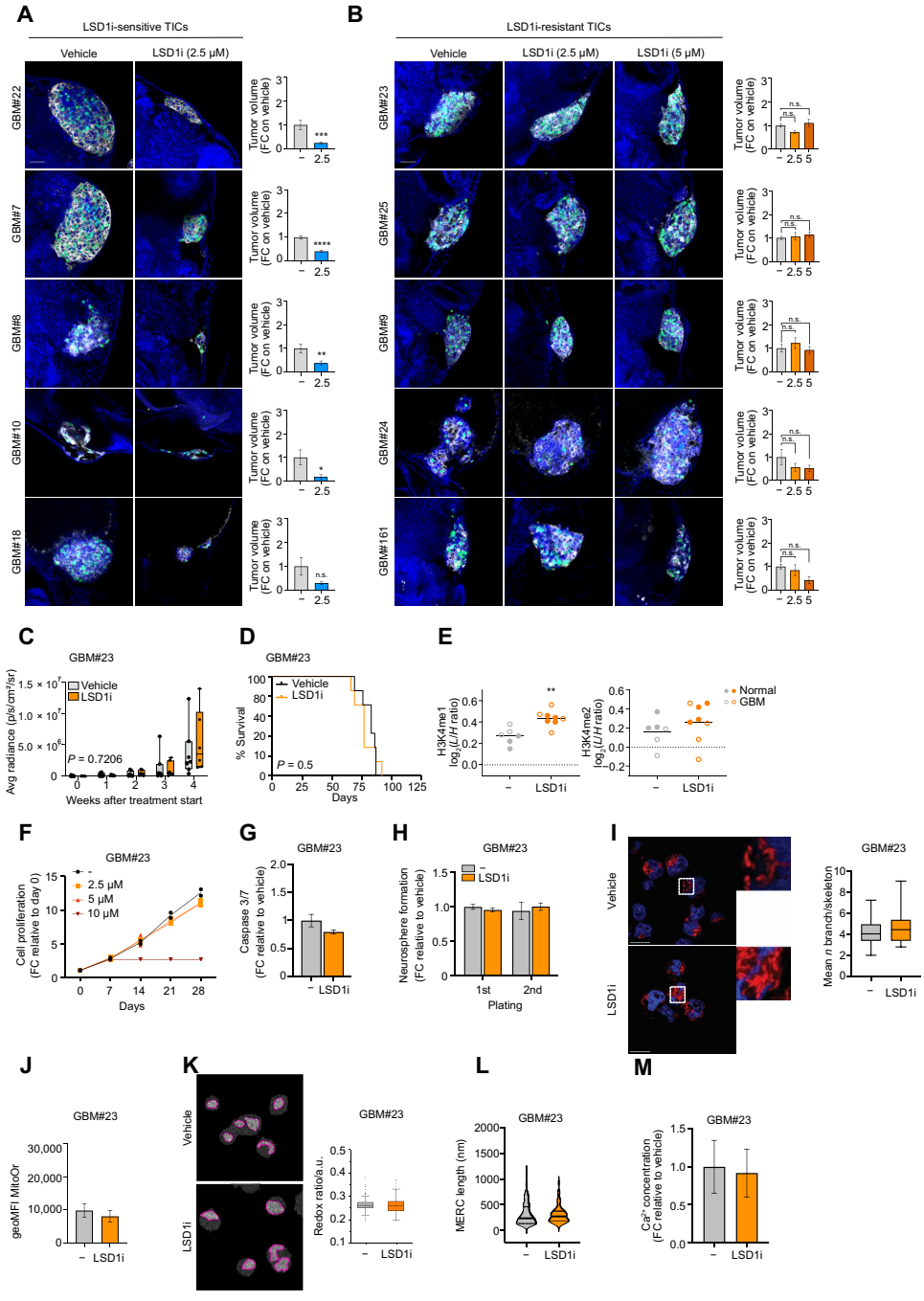

Fig. 3. Interpatient heterogeneity reveals TICs resistant to LSD1i treatment. (**A** and **B**) Representative embryonic zebrafish xenotransplanted with LSD1i-treated (A) LSD1i^{Sens} and (B) LSD1i^{Res} TICs. Tumor volume was quantified. Scale bar, 50 μm (GBM#22: vehicle, $n = 7$ larvae; LSD1i, $n = 9$; GBM#7: vehicle, $n = 10$; LSD1i, $n = 10$; GBM#8: vehicle, $n = 9$; LSD1i, $n = 11$; GBM#10: vehicle, $n = 8$; LSD1i, $n = 6$; GBM#18: vehicle, $n = 8$; LSD1i, $n = 8$; GBM#23: vehicle, $n = 10$; LSD1i_2.5 μM, $n = 9$; LSD1i_5 μM, $n = 9$; GBM#25: vehicle, $n = 9$; LSD1i_2.5 μM, $n = 4$; LSD1i_5 μM, $n = 10$; GBM#9: vehicle, $n = 10$; LSD1i_2.5 μM, $n = 9$; LSD1i_5 μM, $n = 10$; GBM#24: vehicle, $n = 5$; LSD1i_2.5 μM, $n = 6$; LSD1i_5 μM, $n = 5$; GBM#161: vehicle, $n = 8$; LSD1i_2.5 μM, $n = 8$; LSD1i_5 μM, $n = 7$; means ± SEM). (**C**) Normalized bioluminescence (in photons per second per square centimeter per steradian) as a proxy for PDX tumor size (vehicle, $n = 7$; LSD1i, $n = 8$). Avg, average. (**D**) Kaplan-Meyer survival curve of mice as in (C). (**E**) Efficacy of LSD1i in tumors (empty circles) and normal brain (filled circles) from treated PDXs. H3K4me1 and H3K4me2 levels were expressed as *L*/*H* ratios (*L*, sample; *H*, internal standard). (**F**) TIC growth with weekly LSD1i doses ($n = 3$ replicates per group; means ± SD). (**G**) Caspase 3/7 activity ($n = 3$; means ± SD). (**H**) Neurosphere formation efficiency after two propagations ($n = 3$; means ± SD). (**I**) Representative confocal images (left) and quantification (right) of mitochondrial fragmentation. Enlarged highlighted areas (dashed boxes) are shown. Scale bars, 10 μm. ($n = 2$; means ± SD). (**J**) ΔΨm (MitoOr) ($n = 5$; means ± SD). (**K**) Representative images (left) and quantification (right) of redox ratio (vehicle, $n = 175$; LSD1i, $n = 135$ cells; means ± SD). (**L**) MERC length quantification ($n = 20$ cells per condition; means ± SD). (**M**) Ca^{2+} concentration via Rhod-2 fluorescence ($n = 3$; means ± SD). Two-tailed unpaired Student's *t* test, $^*P < 0.05$; $^{**}P < 0.01$; $^{***}P < 0.001$; $^{****}P < 0.0001$ for (A), (E), (G), (J), and (N); Mann-Whitney *U* test, $^{****}P < 0.0001$ for (I), (K), and (M); analysis of variance (ANOVA) for (B), (F), (H), and (L). n.s., not significant.

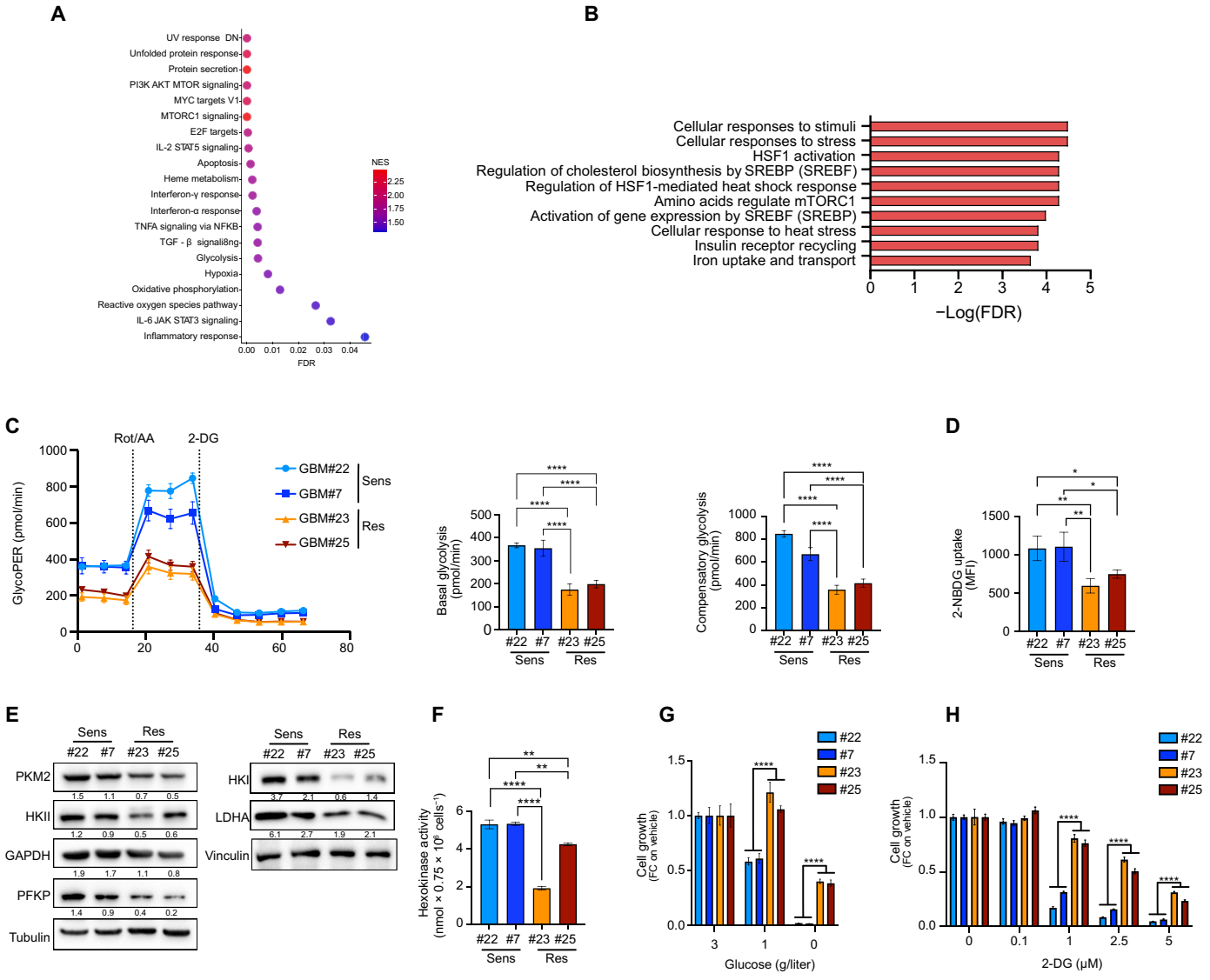

Fig. 4. LSD1i^{Sens} and LSD1i^{Res} TICs display different metabolic features. (**A**) GSEA analysis of hallmarks pathways enriched in LSD1i^{Sens} TICs (GBM#22, GBM#7, GBM#10, GBM#18, and GBM#8) versus LSD1i^{Res} TICs (GBM#23, GBM#9, GBM#24, GBM#161, and GBM#53). The bubble color indicates the NES. UV, ultraviolet; DN, genes downregulated; PI3K, phosphatidylinositol 3-kinase; IL-2, interleukin-2; STAT5, signal transducers and activators of transcription 5; JAK, Janus kinase. (**B**) Pathway enrichment analysis of proteins significantly up-regulated in LSD1i^{Sens} TICs (GBM#22, GBM#7, GBM#10, and GBM#18) compared to LSD1i^{Res} TICs (GBM#23, GBM#9, and GBM#25). The top 10 terms, ranked by FDR, are shown. (**C**) Left: GlycoPER by glycolytic rate assay in LSD1i^{Sens} (GBM#22 and GBM#7) and LSD1i^{Res} (GBM#23 and GBM#25) TICs. Representative kinetic graph (left). Lines indicate the addition of mitochondrial inhibitors Rot/AA and glucose analog (2-DG). Right: Quantification of basal and compensatory glycolysis in the corresponding TICs ($n = 3$; means ± SD). (**D**) 2-NBDG {2-[*N*-(7-nitrobenz-2-oxa-1,3-diazol-4-yl)amino]-2-deoxyglucose} uptake by flow cytometry analysis in GBM TICs ($n = 3$; means ± SD). (**E**) Representative immunoblot of key glycolytic proteins in LSD1i^{Sens} (GBM#22 and GBM#7) and LSD1i^{Res} (GBM#23 and GBM#25) TICs. Vinculin and tubulin are used as loading controls ($n = 2$). (**F**) Hexokinase activity in LSD1i^{Sens} (GBM#22 and GBM#7) and LSD1i^{Res} (GBM#23 and GBM#25) TICs. ($n = 2$; means ± SD). (**G**) Growth of LSD1i^{Sens} (GBM#22 and GBM#7) and LSD1i^{Res} (GBM#23 and GBM#25) TICs under different glucose concentrations ($n = 4$; means ± SD). (**H**) Growth of LSD1i^{Sens} (GBM#22 and GBM#7) and LSD1i^{Res} (GBM#23 and GBM#25) TICs under different concentrations of 2-DG ($n = 4$; means ± SD). ANOVA for (C), (D), and (F) to (H).

Tg-triggered ER stress conditions. The preservation of these features in resistant samples had functional consequences for their survival. Caspase activation was significantly lower in LSD1i^{Res} than in LSD1i^{Sens} TICs upon Tg treatments (Fig. 5C). Similarly, the ER stress inducer TU was more tolerated in LSD1i^{Res} TICs while being highly cytotoxic in LSD1i^{Sens} cells (Fig. 5D). To investigate the ability to recover from acute induction of ER stress, we treated the representative LSD1i^{Sens} GBM#22 TICs and LSD1i^{Res} GBM#25 TICs with Tg for 16 hours, followed by drug washout and monitoring of cell viability for the next 72 hours. As shown in Fig. 5E, viability was severely compromised in Tg-treated GBM#22 TICs, while GBM#25 cells were less affected by this treatment. In accordance, the expression levels of *ATF3*, *CHAC1*, and *DDIT3*, known death-related downstream effectors of the ATF4 pathway (*21*), were significantly higher in LSD1i^{Sens} TICs compared to LSD1i^{Res} TICs. Mechanistically, both LSD1i^{Sens} and LSD1i^{Res} TICs responded to ER stress

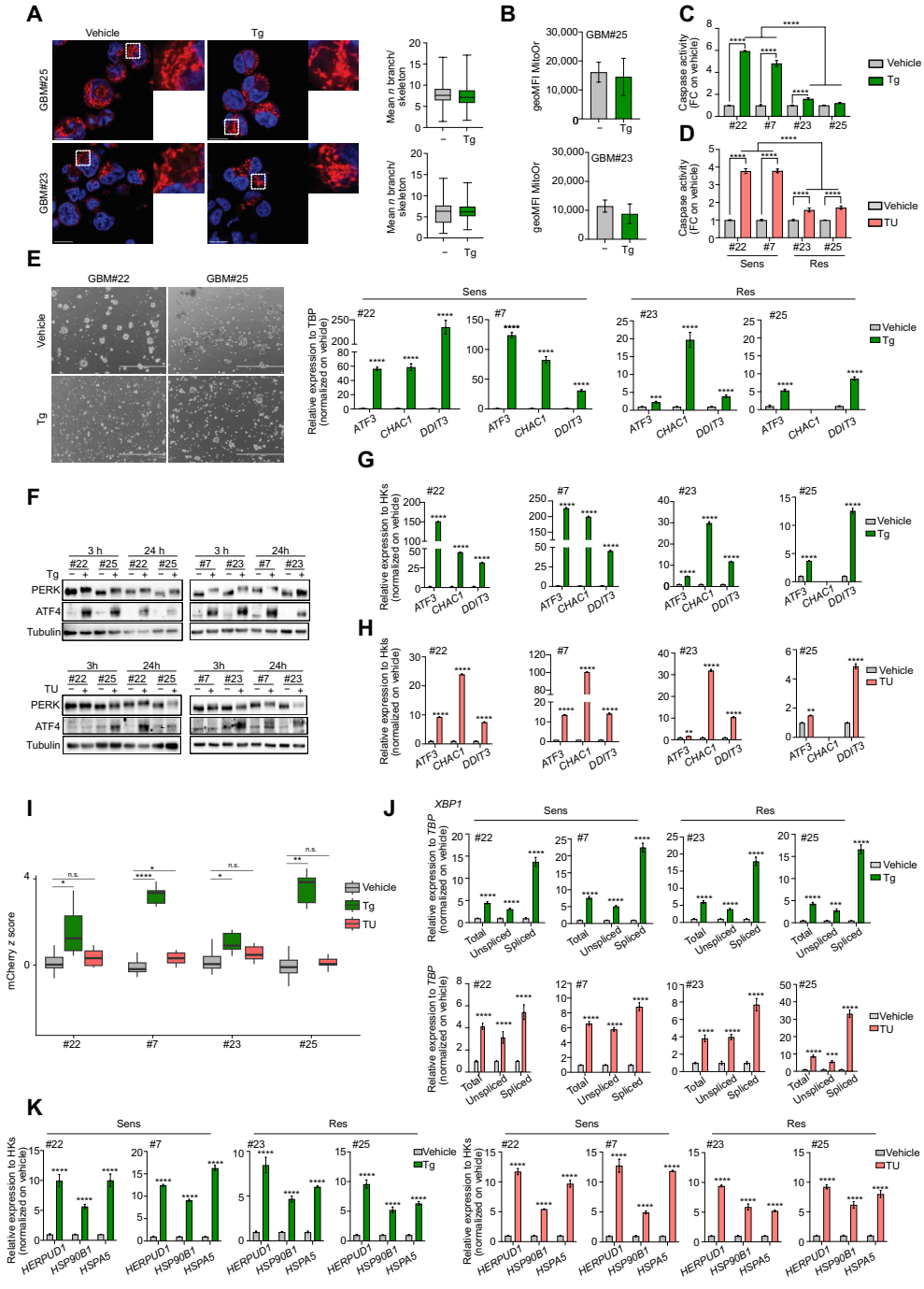

Fig. 5. LSD1i^{Res} TICs maintain mitochondrial integrity to better cope with ER stress. (**A**) Representative confocal images of mitochondrial structure in Tg-treated GBM#23 and GBM#25 TICs (left). Enlarged highlighted areas (dashed boxes) are shown. Mitochondrial fragmentation quantification (right). Scale bars, 10 μm (GBM#25: vehicle, $n = 416$; Tg, $n = 648$; GBM#23: vehicle, $n = 225$; Tg, $n = 326$; means ± SD). (**B**) ΔΨm (MitoOr) after Tg treatment (48 hours) ($n = 3$; means ± SEM). (**C** and **D**) Caspase 3/7 activity in Tg-treated (C) and TU-treated (D) TICs (48 hours) (Tg, $n = 3$; TU, $n = 2$; means ± SD). (**E**) Representative images of GBM#22 and GBM#25 treated with Tg (16 hours) and recovered for 72 hours post-Tg removal. Scale bar, 1000 μm (left). Relative mRNA expression of death-related genes after 72 hours of Tg washout, normalized to TATA box–binding protein (TBP) ($n = 3$; means ± SD). (**F**) Representative immunoblot of PERK-ATF4 axis in LSD1i^{Sens} (GBM#22 and GBM#7) and LSD1i^{Res} (GBM#25 and GBM#23) TICs post-Tg (top) and -TU (bottom) treatments ($n = 3$). Tubulin is used as loading control. h, hours. (**G** and **H**) Relative mRNA expression of death-related genes post-Tg (G) and -TU (H) treatments, normalized to geometric means of housekeeping genes (*TBP*, *GAPDH*, *RPLPO*, and *18S*) ($n = 3$ replicates per group means ± SD). (**I**) Representative bar plot showing means mCherry fluorescence intensity post-Tg and -TU treatments. (**J**) Relative mRNA expression of *XBP1* gene (total, unspliced, and spliced form) post-Tg and -TU treatments, normalized to *TBP* ($n = 3$ replicates per group; means ± SD). (**K**) Relative mRNA expression of ATF6 target genes post-Tg and –TU treatments, normalized to geometric means of housekeeping genes (*TBP*, *GAPDH*, *RPLPO*, and *18S*) ($n = 3$ replicates per group; means ± SD). Mann-Whitney *U* test for (A). Two-tailed unpaired Student's *t* test, $^{**}P < 0.01$; $^{***}P < 0.001$; $^{****}P < 0.0001$ for (B), (E), (G), (H), (J), and (K); ANOVA, $^{*}P < 0.05$; $^{**}P < 0.01$; $^{****}P < 0.0001$ for (C), (D), and (I).

induced by either short-term (3 hours) or prolonged (24 hours) Tg or TU treatment (Fig. 5F). The phosphorylation of PERK (RNA-activated protein kinase–like ER kinase) and the subsequent induction of ATF4 occurred in both LSD1i^{Sens} (GBM#22 and GBM#7) and LSD1i^{Res} (GBM#23 and GBM#25) TICs, indicating the activation of the PERK arm of the UPR pathway in both cell groups. Notably, the expression of the ATF4 proapoptotic effectors was significantly higher in LSD1i^{Sens} than in LSD1i^{Res} TICs upon either Tg (Fig. 5G) or TU (Fig. 5H) treatment. Regarding the inositol-requiring enzyme 1α (IRE1α) branch of the UPR, we used a previously validated reporter construct containing the *XBP1* promoter region fused to mCherry (*52*) and measured mCherry fluorescence in response to Tg and TU treatment. Both LSD1i^{Sens} and LSD1i^{Res} TICs exhibited a significant increase in mCherry fluorescence intensity in response to Tg, with only minor reporter activation observed upon TU treatment (Fig. 5I). Upon activation of the IRE1α-XBP1 pathway, *XBP1* mRNA is spliced by IRE1α. The increased expression of the spliced isoform of *XBP1* mRNA in Tg- or TU-treated LSD1i^{Sens} and LSD1i^{Res} TICs further demonstrated that IRE1α-XBP1 pathway was activated in both samples in response to ER stress (Fig. 5J). In addition, we measured the upregulation of homocysteine-inducible ER protein with ubiquitin-like domain 1 (*HERPUD1*), heat shock protein 90β family member 1 (*HSP90B1*), and heat shock protein family A (*Hsp70*) member 5 (*HSPA5*) (Fig. 5K), known ATF6 target genes (*53*), in response to Tg and TU treatment in both LSD1i^{Sens} and LSD1i^{Res} TICs.

Collectively, the lack of compromised mitochondrial morphology and membrane potential upon ER stress induction in LSD1i^{Res} TICs suggests that these cells are likely to exploit mechanisms that maintain mitochondrial integrity and function under stress conditions, enabling them to better withstand ER stress compared to LSD1i^{Sens} TICs. The responses to Tg and TU treatment demonstrate that the UPR pathway can be similarly activated in both LSD1i^{Ses} and LSD1i^{Res} cells. However, while the induction of ATF4 leads to the death of LSD1^{Sens} TICs, in LSD1^{Res} TICs, it likely initiates an adaptive response aimed at restoring homeostasis.

LSD1i induces PERK accumulation and alters PERK-mediated stress responses

By examining the molecular indicators of ER stress upon LSD1i treatment, we found that PERK protein was consistently accumulated in LSD1i-treated LSD1i^{Sens} TICs from various patients (GBM#22, GBM#7, GBM#8, and GBM#18) compared to vehicle-treated cells (Fig. 6A). Notably, the effect of LSD1i mirrored that resulting from the combination of Tg and GSK2606414 PERK inhibitor (here PERKi) (Fig. 6B). While Tg treatment led to PERK oligomerization and phosphorylation, as revealed by the PERK protein shift (Fig. 6A), the treatment of Tg-exposed TICs with PERKi almost completely inhibited PERK autophosphorylation (Fig. 6B), as previously published (*54*). We observed that PERK accumulation in LSD1i^{Sens} TICs occurred after 24 hours of LSD1i treatment (Fig. 6C) and was maintained over time (Fig. 6, A and C).

The analysis of previously published LSD1 chromatin immunoprecipitation sequencing in GBM-TICs (*21*) showed that LSD1 binds to the *PERK* promoter region, and that LSD1i treatment results in increased levels of H3K4me2 and H3K4me3 at these sites (fig. S5A). However, despite the augmented PERK protein expression following LSD1i treatment, the raise in these methylation marks were not directly associated with changes in gene expression (fig. S5B).

As expected, LSD1i treatment did not affect PERK in resistant samples (Fig. 6A). We observed no differences after LSD1i treatment in IRE1α phosphorylation (fig. S5C), IRE1α-mediated XBP1 activation (fig. S5D), and ATF6 target genes expression (fig. S5E) in both LSD1i^{Sens} and LSD1i^{Res} TICs. Overall, the convergence of the effects of LSD1i and Tg/PERKi combination on PERK accumulation in LSD1i^{Sens} TICs indicates a dysregulation of the PERK-mediated responses to ER stress.

PGAP1 is a key mediator of LSD1i resistance

We demonstrated that LSD1i triggers an ER stress response that collectively affects ER homeostasis and mitochondrial dynamics and function. Moreover, the specific metabolic features of LSD1i^{Sens}

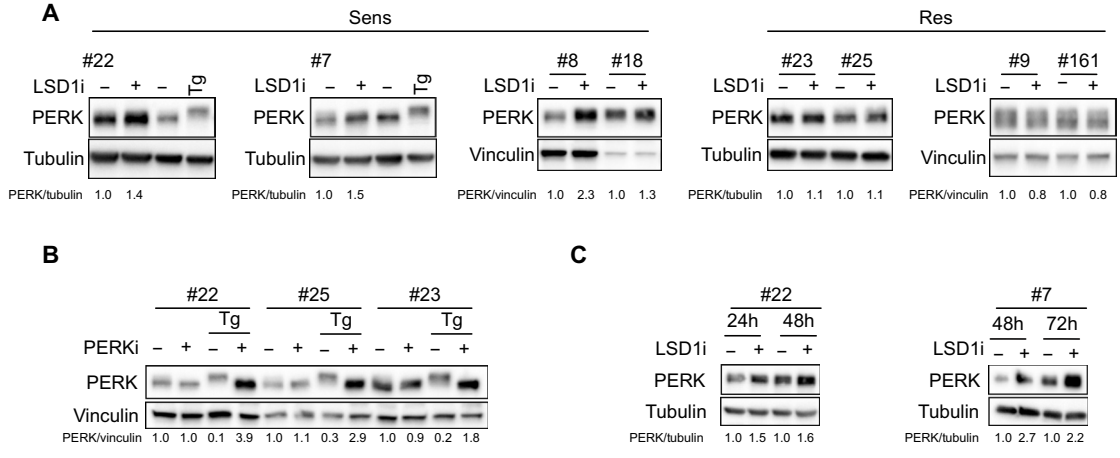

Fig. 6. LSD1i induces PERK accumulation and alters PERK-mediated stress responses. (**A**) Representative immunoblot of PERK protein expression in LSD1i^{Sens} (GBM#22, GBM#7, GBM#8, and GBM#18) and LSD1i^{Res} (GBM#25, GBM##23, GBM#9, and GBM#161) TICs upon LSD1i treatment. Tubulin or vinculin is used as loading control. Tg-treated TICs are used as positive controls to measure the oligomerization/autophosphorylation of PERK ($n = 3$). (**B**) Representative immunoblot of PERK protein level in a panel of TICs treated with Tg and GSK2606414 (PERKi), either individually or in combination. Vinculin is used as loading control ($n = 3$). (**C**) Representative immunoblot of PERK in LSD1i^{Sens} (GBM#22 and GBM#7) TICs after LSD1i treatment at the indicated time points. Tubulin is used as a loading control. In (A) and (C), protein signal quantification are normalized to tubulin or vinculin and expressed as fold change (FC) relative to the untreated condition for each TIC.

TICs and LSD1i^{Res} TICs are likely responsible for the maladaptive UPR response in the former and the adaptive UPR response in the latter. Stemming from this evidence, we screened LSD1i^{Res} TICs with a metabolic short hairpin RNA (shRNA) library targeting genes involved in key metabolic pathways (table S2), attempting to identify potential vulnerabilities or dependencies in LSD1i^{Res} samples likely conferring resistance to LSD1i.

Upon lentiviral transduction and puromycin selection, the representative patient-derived LSD1i^{Res} GBM#23 TICs were treated with LSD1i (2.5 and 5 μM) or vehicle. By comparing LSD1i-treated and control cells, we identified 14 synthetic lethality hits that were depleted under treated conditions, in common to at least two of four replicates, and not counterselected under the control condition (fig. S6A). Our attention turned to post–glycosylphosphatidylinositol (GPI) attachment to proteins inositol deacylase 1 (PGAP1). PGAP1 resides in the ER where it contributes to the maintenance of ER homeostasis mediating posttranslational modifications, maturation, and sorting of GPI-anchored proteins (GPI-APs) (*55*, *56*). The impairment of PGAP1 function affects the proper export of GPI-APs from ER to the cell surface (*57*). Moreover, PGAP1 is involved in the quality control mechanisms for GPI-APs by promoting the degradation of misfolded ones. Thus, its dysfunction leads to the accumulation of misfolded proteins potentially contributing to the onset of ER stress (*58*). To date, no studies explore the role of PGAP1 in GBM. In silico data showed that *PGAP1* is overexpressed in GBM compared to the normal brain (Fig. 7A). By assessing its expression in multiple patient-derived TICs, we found that the mRNA expression of *PGAP1* was higher in LSD1i^{Res} TICs compared with LSD1i^{Sens} samples (Fig. 7B). Moreover, the segregation of glioma tissues from The Cancer Genome Atlas (TCGA) database based on *PGAP1* mRNA levels revealed that GBMs with low *PGAP1* expression showed significant enrichment in TNF-α and NF-κB pathways, hypoxia, interferon response, glycolysis, OXPHOS, and apoptosis (Fig. 7C), all of which were associated with sensitivity to LSD1i (Fig. 4A).

To investigate the functional role of PGAP1 in GBM TICs, we knocked down *PGAP1* expression in two different patient-derived LSD1i^{Res} TICs (GBM#23 and GBM#25) with distinct shRNAs (sh#1, sh#3, and sh#57) cloned in lentiviral vectors (Fig. 7D and fig. S6B). Our findings indicate that *PGAP1* silencing reduced neurosphere-forming capacity of both TIC samples (Fig. 7E and fig. S6C). Of relevance, the combination of *PGAP1* knockdown with LSD1i further affected the self-renewal of LSD1i^{Res} TICs (Fig. 7E and fig. S6C). Accordingly, the overexpression of *PGAP1* cDNA in PGAP1-silenced cells (fig. S6D) reversed the PGAP1 knockdown–induced inhibition of cell growth in LSD1i^{Res} TICs and restored the resistance to LSD1i treatment (fig. S6E). *PGAP1* silencing alone did not significantly affect ΔΨm (Fig. 7F and fig. S6F). Nevertheless, LSD1i treatment in PGAP1-silenced TICs led to a significant hyperpolarized ΔΨm (Fig. 7F and fig. S6F), mirroring the response induced by LSD1i in LSD1i^{Sens} TICs (Fig. 1 and fig. S1). Treatment with TMZ alone closely mirrored the inhibitory effect of LSD1i on PGAP1-silenced TIC growth (Fig. 7G). Notably, the combined treatment with LSD1i and TMZ resulted in additive growth inhibition of LSD1i^{Res} PGAP1-silenced TICs (Fig. 7G). We next extended our in vitro findings to in vivo GBM models. We intracranially implanted luciferase-positive PGAP1-silenced and control GBM#23 TICs into immunocompromised mice. After 6 weeks, the necessary time for tumor formation, mice were randomly divided into four groups and treated with LSD1i as already described (*21*). Tumor growth, as assessed by bioluminescence imaging, was significantly reduced in mice transplanted with PGAP1-silenced TICs. Notably, we found a more pronounced effect when combined with LSD1i treatment (2 weeks after LSD1i administration), although this combination did not achieve an ideal therapeutic effect (Fig. 7, H and I). When LSD1i treatment was interrupted after 4 weeks, tumor masses continued to increase. This aligns with our previous demonstration that inhibition of in vivo GBM outgrowth diminishes after the suspension of LSD1i treatment (*21*). By 6 weeks after LSD1i administration, when *PGAP1* was still silenced in the tumor area (Fig. 7J), the average tumor burden in both LSD1i-treated and vehicle-treated PGAP1-silenced PDXs became comparable (Fig. 7, H and I). PGAP1-silenced PDXs displayed significantly smaller tumors than mice bearing control PDXs over the whole experiment (Fig. 7, H and I). Consistent with these results, *PGAP1* silencing prolonged the survival of GBM PDXs (Fig. 7K). Overall, these data suggest that PGAP1 per se plays a critical role in TIC maintenance and likely has a priming effect on ER and mitochondrial homeostasis and function. PGAP1 targeting creates a vulnerability in LSD1i-resistant TICs that enhances their responsiveness to LSD1i treatment and even enhances TIC sensitivity to TMZ, further supporting the translational relevance of this combination strategy.

DISCUSSION

We have previously reported that LSD1-directed treatment shows therapeutic benefits in GBM TICs (*21*). Our findings reveal heterogeneity in the response to LSD1i treatment across different GBM TIC samples. Sensitivity to LSD1i occurs in a specific subset of GBM TICs with enhanced glycolytic activity. In these samples, LSD1i treatment is associated with multiple stress conditions, including perturbations in mitochondrial dynamics and metabolism, disruption of Ca^{2+} homeostasis, and redox imbalance, which, in turn, affects ER homeostasis. This specific subpopulation of GBM TICs is highly sensitive to ER stress–inducing agents that disrupt mitochondrial function and ER homeostasis.

Mitochondria are intracellular organelles with a relevant role in cell survival, energy production, and adaptation to stress (*39*). Because of the high energy demands of GBM TICs and their need to cope with the harsh conditions of the brain tumor microenvironment—including hypoxia, nutrient deprivation, and resistance to therapy—maintaining proper mitochondrial function is essential. LSD1i alters mitochondrial structure and function, inducing apoptosis by hyperpolarizing the mitochondrial membrane, increasing the redox ratio, and releasing cytochrome c. These changes disrupt both OXPHOS and glycolysis, reducing ATP production and TIC survival. Similar mitochondrial alterations have been observed in cells under stress conditions, such as oxidative stress (*36*), hypoxia (*59*), drug exposure (*45*), and in cells committed to death (*35*). Furthermore, these changes can be associated with additional characteristic rearrangements, including increased levels of MFN1 and MFN2 (*60*), a hyperpolarized ΔΨm, and an enhanced mitochondrial redox ratio (*36*), all of which affect cell viability. This mitochondrial remodeling promotes the release of proapoptotic factors such as cytochrome c (*61*), amplifying apoptosis through caspase activation and mitochondrial DNA fragmentation (*62*).

Mitochondrial structural changes are associated with their dysfunction. Our data show that LSD1i treatment reduces OXPHOS in GBM TICs, significantly decreasing mitochondrial ATP production. Notably,

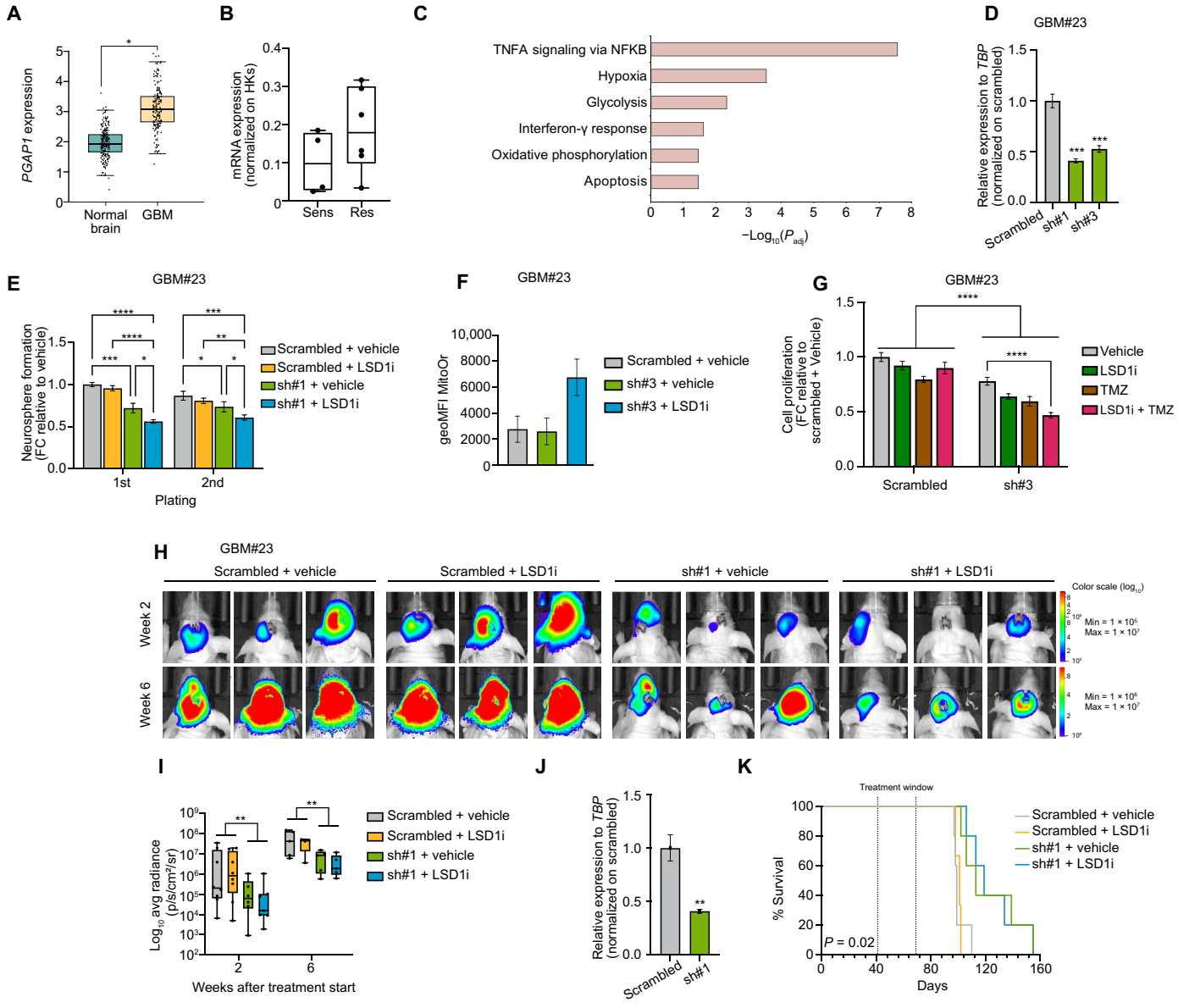

Fig. 7. PGAP1 is a key mediator of LSD1i resistance. (**A**) *PGAP1* mRNA expression level in GBM tissues and normal brain using the GEPIA2, TCGA and GTEx databases. TPM, transcripts per million. (**B**) Relative *PGAP1* mRNA expression in LSD1i^{Sens} (GBM#22, GBM#7, GBM#10, and GBM#8) and LSD1i^{Res} (GBM#23, GBM#9, GBM#25, GBM#24, GBM#20, and GBM#161) TICs, normalized to geometric means of housekeeping genes (*TBP*, *GAPDH*, *RPLPO*, and *18S*) ($n = 2$; means ± SD). (**C**) GSEA of hallmark pathways in low ($n = 16$) versus high ($n = 20$) *PGAP1*-expressing GBM tissues from TCGA. (**D**) Efficiency of *PGAP1* silencing (sh#1 and sh#3) compared to control (scrambled), normalized to *TBP*. (**E**) Neurosphere formation efficiency after *PGAP1* silencing (sh#1) in combination with LSD1i. Two serial neurosphere propagations were assessed ($n = 2$; means ± SD). (**F**) ΔΨm (MitoOr) in PGAP1-silenced GBM#23 TICs (sh#3) after LSD1i ($n = 3$; means ± SEM). (**G**) Growth of PGAP1-silenced and control TICs treated with LSD1i, TMZ, or their combination. (**H**) Representative images of mice transplanted with PGAP1-silenced (shPGAP1) or control TICs, treated with LSD1i or vehicle. Treatment began 6 weeks post-TIC implantation (scrambled + vehicle, $n = 8$; scrambled + LSD1i, $n = 7$; sh#1 + vehicle, $n = 6$; sh#1 + LSD1i, $n = 7$). Bioluminescence imaging at time points is shown. (**I**) Normalized bioluminescence (in photons per second per square centimeter per steradian) as a proxy for tumor size in mice as in (H). (**J**) *PGAP1* expression in PGAP1-silenced (sh#1) and control (scrambled) PDXs, 5 weeks after LSD1i administration, normalized to *TBP*. (**K**) Kaplan-Meyer survival curve for the treated mice as in (G) and (H). Survival differences were compared by log-rank test. Mann-Whitney *U* test, $^*P < 0.05$ for (A). Two-tailed unpaired Student's *t* test, $^{***}P < 0.001$ for (B) and (D). ANOVA, $^*P < 0.05$; $^{**}P < 0.01$; $^{***}P < 0.001$; $^{****}P < 0.0001$ for (E) and (F).

LSD1i treatment also impairs the glycolytic activity of GBM TICs, leading to a concurrent reduction in glycolytic ATP production. This marked depletion of global ATP ultimately affects the survival of TICs, as previously demonstrated (*21*). Supporting these findings, we identified a strong and significant correlation between LSD1 expression and both glycolysis- and OXPHOS-related gene signatures in patients with GBM from the CGGA and Gravendeel cohorts (*43*) These findings confirm LSD1's crucial role in regulating cell metabolism, including glucose uptake, oxygen consumption, extracellular acidification, and the metabolic shift between glycolysis and OXPHOS (*22*, *63*, *64*).

LSD1i-induced mitochondrial dysfunctions and glycolytic impairment may trigger ER stress and ATF4 induction in GBM TICs.

Different studies link ATF4 induction to mitochondrial stress and metabolic reprogramming (*65*, *66*). Reduced glycolysis and weakened oxidative metabolism, as well as lower ATP levels, are associated with ATF4 stress granules (*30*, *67*), markers of ISR-ATF4 activation. Moreover, mitochondrial inhibitors commonly induce ATF4 induction (*34*). ER stress also affects mitochondrial morphology and function as an adaptive strategy. It has been reported that ER stress affects mitochondrial dynamics and glycolysis in cancer cells. Initially, it causes mitochondrial fragmentation, MERC formation (*68*), and Ca^{2+} influx, followed by an adaptive phase where a mitochondrial network is reestablished to improve OXPHOS efficiency. Prolonged ER stress, however, leads to excessive Ca^{2+} transfer via MERCs, disrupting the mitochondrial network and triggering apoptosis (*44*, *69*–*72*). Dysregulated Ca^{2+} signaling further inhibits glycolysis and induces apoptosis, as seen in breast (*73*) and neuroblastoma cancer cells (*74*). Notably, LSD1i-treated TICs show increased MERCs and intracellular Ca^{2+} overload, with elevated MFN1 and MFN2 levels indicating enhanced ER-mitochondrial coupling and mitochondrial remodeling (*75*, *76*).

LSD1 activity has previously been linked to the UPR pathway activation, as well as ER and oxidative stress conditions in cancer, including GBM (*21*, *77*, *78*). In the GBM context, LSD1inhibitors (NCL-1 and NCD-38) reduce glioma stem cell viability and neurosphere formation by activating the UPR pathway (*79*). The LSD1i DDP38003 used here synergized with stressors to induce a maladaptive ISR, culminating in the enrichment of death-related genes associated with the UPR and ER stress response (*21*). Our findings show that LSD1i induces a stress response in GBM TICs, resembling the effects of the ER stress inducers Tg and TU. These well-known stressors disrupt mitochondrial structure and function, activate stress granule formation, and up-regulate ATF4 and its proapoptotic genes. The key distinction is that while LSD1i induces a similar ER stress response, its progression is slower compared to the rapid effects of Tg and TU. This prolonged ER stress disrupts cellular energy production by reducing both glycolytic and mitochondrial activities, leading to lower ATP levels. The cumulative impact of these disruptions is the eventual cell death of GBM TICs.

GBM TICs show heterogeneity in response to LSD1i. LSD1i^{Res} TICs maintain cell proliferation, self-renewal, metabolism, and ER-mitochondrial coupling despite LSD1i treatment, as confirmed in zebrafish and mouse models. As for those TICs responsive to LSD1-directed therapy (*21*), resistance to LSD1i was independent of molecular subtyping or genomic alterations. Analysis of transcriptomic data and extracellular flux results reveals that LSD1i^{Sens} TICs rely primarily on high glycolytic activity for growth. Inhibiting glucose metabolism, either by glucose deprivation or by 2-DG treatment, significantly impaired their growth. In contrast, LSD1i^{Res} TICs exhibit reduced basal glycolytic activity, similar basal OCR, and do not depend on specific metabolic pathways (fig. S4).

A distinct feature of TICs is their metabolic flexibility, allowing them to adapt to various bioenergetic stresses, and often linked to resistance to radiochemotherapies (*80*, *81*). In agreement with their lower glycolytic activity, LSD1i^{Res} TICs showed reduced susceptibility to glucose deprivation or glycolysis inhibition, likely surviving using alternative metabolites and metabolic pathways. In this context, assessing alternative metabolic fuel utilization in these cells would provide deeper insights into their adaptive mechanisms. GL261 cells clustered with LSD1i^{Res} samples not only for their in vitro/in vivo insensitivity to LSD1i but also for their low glycolytic phenotype, which enables long-term survival under glucose starvation (*82*). Similar to LSD1i, Tg did not significantly affect mitochondrial dynamics, morphology, or the overall survival of LSD1i-resistant TICs. This suggests that maintaining intact mitochondrial function and ER homeostasis serves as a protective mechanism for LSD1i-resistant TICs, shielding them from cell death caused by LSD1i treatment or stronger chemical stressors. Furthermore, this highlights their enhanced resistance to ER stress.

The ER stress response is mediated by three key receptors in the ER: PERK, ATF6, and IRE1α. Our study found that while both LSD1i^{Sens} and LSD1i^{Res} TICs perceive stress induced by Tg or TU, their responses are different. LSD1i^{Sens} cells undergo cell death, whereas LSD1i^{Res} samples activate adaptive UPR signaling for recovery. LSD1i induces PERK protein accumulation in LSD1i^{Sens} TICs without activating its kinase function, mimicking the effects of the PERKi GSK2606414 during Tg treatment (*54*). PERK plays a critical role in stress monitoring, through dimerization/oligomerization and autophosphorylation. Inhibition of PERK kinase activity by GSK2606414 during ER stress disrupts protein maturation and causes retention in the ER (*54*), increases mitochondrial fragmentation, and impairs mitochondrial respiration (*83*). These phenotypes are mirrored by PERK genetic targeting (*83*), which also alters ER and mitochondrial networks and disrupts Ca^{2+} and redox signaling (*84*). PERK's role in modulating mitochondrial dynamics and maintaining ER homeostasis is linked to its localization at MERCs (*69*, *85*). The existence of a cross-talk between the branches of the UPR is reported (*86*). However, the activation of IRE1α or overexpression of ATF6 target genes did not occur in either LSD1i^{Sens} or LSD1i^{Res} TICs upon LSD1i treatment. Although we report that LSD1 binds the PERK gene promoter and increases H3K4me2 and H3K4me3 marks at the LSD1-bound PERK promoter upon LSD1i treatment, LSD1 does not regulate PERK expression at the transcriptional level. This is consistent with our previous findings that LSD1 catalytic activity inhibition is independent of changes in gene expression or chromatin accessibility in GBM TICs (*21*).

We highlight that in LSD1i^{Sens} TICs, LSD1i treatment disrupts PERK signaling, likely affecting ER homeostasis and stress transmission to the mitochondria, leading to mitochondrial dysfunction. However, LSD1i^{Res} TICs do not exhibit a specific energetic dependency and can adaptively regulate UPR to restore ER and mitochondrial homeostasis even under stronger stressors such as Tg. Therefore, targeting this adaptive mechanism could be crucial for sensitizing these cells to LSD1i and other ER stress–inducing treatments. Among the few synthetic lethality hits identified, we focused on PGAP1, an ER localized protein essential for processing GPI-APs (*55*–*57*). Dysfunction in PGAP1 leads to the accumulation of misfolded proteins, contributing to ER stress (*58*). Although PGAP1 has no established link to cancer, including GBM, it is associated with neurological disorders such as intellectual disability (*87*–*89*). GPI-APs have demonstrated protumorigenic roles in various cancers (*90*–*92*). Our findings reveal that PGAP1 contributes to intrinsic resistance to LSD1i. Silencing *PGAP1*, either alone or in combination with LSD1i, disrupted the maintenance of LSD1i^{Res} TICs, suggesting that targeting ER homeostasis could eradicate these cells. While no PGAP inhibitors currently exist, its recently structural characterization provides opportunities for drug development (*93*). Analysis of GBM patient data identified two groups, PGAP1^{Low} and PGAP1^{High}. PGAP1^{Low} tumors showed transcriptome profiles resembling LSD1i^{Sens} TICs, while LSD1i^{Res} TICs are likely to exploit PGAP to maintain ER homeostasis

under therapy-induced stress. Disrupting this mechanism by PGAP1 targeting could impair TIC adaptability and sensitize them to treatments such as TMZ. Furthermore, combining the PGAP1-targeting strategy with LSD1i DDP_38003 is likely to enhance the effectiveness of TMZ, providing a robust approach for tackling the aggressive nature of GBM TICs. The translational relevance of this strategy is further strengthened by recent preclinical results from the Sareddy group, which demonstrated the efficacy of NCD-38 LSD1i to enhance TMZ efficacy against GBM TICs (*94*).

In addition to PGAP1, our synthetic lethal screen identified several promising candidates, including genes involved in glutamine metabolism (*GLS* and *GLS2*), lipid metabolism (*MTMR14* and *INPP4A*), nucleotide biosynthesis (*RRM2B*, *TRDMT1*, and *ADSS*), and protein ubiquitination and folding (TRIM47, TRIM8, CHST13, BIRC3, TRIM37, and UBR5). Some of them have protumorigenic functions in various cancer models (*95*–*97*), with BIRC3, GLS, and RRM2B involved in GBM development and therapeutic resistance (*98*–*100*). Inhibitors targeting several of these genes are already in clinical trials (*101*).

Building on our previous findings that LSD1 inhibition impairs GBM TICs' ability to overcome stress by disrupting the LSD1-CBP-ATF4 signaling axis (*21*), our results link LSD1-directed therapy to managing adaptive or maladaptive ER stress depending on the metabolic characteristics of patient-derived TICs. To improve TIC-specific treatments, combinatorial strategies with LSD1i and inhibitors targeting either glycolysis or OXPHOS metabolism could significantly restrict GBM tumor evolution by limiting TIC metabolic plasticity and preventing potential compensatory metabolic mechanisms. Likewise, interference with the proper maintenance of mitochondrial function and ER homeostasis might be exploited to target treatment-resistant TICs, such as those escaping LSD1i, glucose deprivation, or glycolysis inhibition with 2-DG. These insights underscore the therapeutic potential of targeting GBM metabolism to enhance treatment efficacy.

Limitations of the study

In this study, we demonstrated that enhanced glycolytic activity in GBM TICs underlies the efficacy of LSD1i-directed therapy. In contrast, $LSD1^{Res}$ TICs, which have lower glycolytic activity and greater resistance to glucose deprivation or glycolysis inhibition, rely on increased mitochondrial adaptability for their survival. Although various LSD1is have been developed, only few have advanced to clinical trials (*102*). However, their application in GBM has yet to achieve comparable success, with preclinical research still focusing on optimizing compounds to effectively target GBM cells and, particularly, GBM TICs (*103*, *104*). These inhibitors differ in their mechanisms of action (catalytic versus scaffolding), reversibility (reversible versus irreversible inhibition), target modulation, brain tissue penetration, and toxicity profiles, all of which influence their therapeutic potential. Notably, tumor regrowth has been observed even after prolonged LSD1 pharmacological inhibition (*103*, *104*), highlighting the importance of exploring alternative DDP_38003 administration regimens, not only in samples sensitive to LSD1i but also in LSD1i-resistant GBMs. In this context, further investigation is necessary for the "LSD1i + PGAP1 silencing" combination strategy to reach its full potential, including the development of therapeutic agents targeting PGAP1 function and comprehensive in vivo studies. To understand the adaptive mechanisms underlying GBM-resistant phenotype, future research should investigate the alternative metabolic fuels these cells may use, particularly in the context of LSD1-directed therapy or other ER stress agents. Of particular interest would be the evaluation of amino acids such as glutamine as alternative fuels. In this regard, GLS, the mitochondrial enzyme that converts glutamine into glutamate, feeding into the trichloroacetic acid cycle, emerged as a potential target from the synthetic lethal screen. Since GLS is involved in maintaining cellular energy and metabolic precursors, investigating its role both independently and in combination with LSD1i could uncover new therapeutic opportunities. In addition, a comprehensive metabolomic analysis would provide valuable insights into how both $LSD1^{Sens}$ and $LSD1^{Res}$ TICs manage metabolic stress. Last, although our results suggest that PERK contributes to the cellular response to ER stress, further investigations are needed to determine whether PERK activity or expression is regulated through an LSD1-dependent epigenetic mechanism or by LSD1's scaffolding function.

MATERIALS AND METHODS

Experimental design

This study aimed to explore the mechanisms underlying sensitivity and resistance to LSD1i. TICs from different GBM patient specimens, orthotopic GBM PDXs, and GBM zebrafish models were used for in vitro and in vivo experiments. LSD1i and various chemical stressors were applied to assess stress response activation and adaptations in GBM TICs. Metabolic-based assays were used to identify specific metabolic features associated with sensitivity or resistance to LSD1i therapy, with the goal of developing strategies to target LSD1i-resistant cells. Biological replicates are indicated in figure legends. Animal experiments were randomized and evaluated by two blinded operators, and a minimum of three mice per group was chosen on the basis of preliminary data to ensure statistical significance.

GBM patient-derived TIC cultures

GBM TICs were isolated from specimens of different patients with GBM, as already described (*105*). They were grown and maintained as 3D spheroid aggregates in serum-free DMEM/F12 medium (Dulbecco's modified Eagle medium/Ham's F12 nutrient mixture; Gibco) supplemented with B27 supplement (X1; Life Technologies), human epidermal growth factor (20 ng/ml), human basic fibroblast growth factor (10 ng/ml; PeproTech), 2 mM L-glutamine, and 1% penicillin/streptomycin. No specific cell subpopulations were isolated on the basis of surface marker expression. Spheres were passaged by mechanically dissociation every 5 to 7 days when they reached ~300 to 500 μm in diameter. TIC cultures were used within 30 passages from their establishment and were routinely tested for *Mycoplasma* contamination. Cells were maintained at 37°C in a 5% CO_2-humidified incubator. Information for each patient-derived TIC culture is provided in table S1.

Mouse models of GBM

Orthotopic implantation of either GBM TICs or GL261 cells was carried out as previously described (*1*). Briefly, 100.000 cells were suspended in 2 μl of phosphate-buffered saline (PBS) and stereotaxically injected into the nucleus caudatus (coordinates from bregma: 1 mm posterior, 3 mm left lateral, 3.5 mm in depth) of 4- to 6-week-old female CD-1 mice for GBM TICs or 4- to 6-week-old female C57BL/6 mice for GL261 cells (Charles River, Wilmington, MA). Tumor-bearing mice were monitored daily for the development of neurological symptoms.

For LSD1i administration, CD-1 mice were treated with LSD1i (17 mg/kg) twice a week for 4 weeks by oral gavage, starting 6 weeks after GBM#23 injection. C57BL/6 mice received LSD1i (34 mg/kg) for 2 weeks, beginning the first week after GL261 injection.

Bioluminescence measurements were performed by intraperitoneal injection D-luciferin firefly (PerkinElmer, France) at a dose of 150 mg/kg of body weight. Acquisitions started 10 min after injection, in animal under gas anesthesia (2% isoflurane). Imaging and data processing were performed using PerkinElmer's IVIS Lumina Series III instrument wavelengths (600 to 800 nm; PerkinElmer, France).

All experiments in mice were performed in accordance with protocols approved by the Italian Ministry of Health (authorization no. 556/2016-PR), in compliance with Italian laws (D.L. vo 116/92 and subsequent amendments), which enforce EU directive 86/609 (council directive 86/609/EEC).

Zebrafish models of GBM

Xenotransplantation was performed on wild-type AB zebrafish (*Danio rerio*) larvae at 2 days postfertilization (dpf). GBM TICs transduced with histone 2B–green fluorescent protein (H2B-GFP) lentivirus were collected after a 3-day treatment with 2.5 μM LSD1i or upon lentiviral-mediated LSD1 silencing (sh#71) and resuspended at 10^5 cells/μl in medium. Larvae at 2 dpf were anesthetized with 0.016% ethyl-3-aminobenzoate methane-sulfonate salt (Sigma-Aldrich), and pigmentation was inhibited by 0.003% *N*-phenylthiourea (Sigma-Aldrich) in embryo medium. Xenotransplantation was performed by loading the cell suspension into custom microinjection needles, prepared by pulling glass capillaries (GC100T-15, Harvard Apparatus). Each larva was injected with 5 nl of cell suspension, corresponding to 500 cells, using a manual micromanipulator (Narishige). Cells were transplanted subcutaneously into the perivitelline space. Larvae were immediately selected for correct transplantation with a Nikon SMZ25 stereomicroscope. Only correctly injected larvae were maintained at 34°C and screened at 3 days postinjection. Ex vivo analyses were performed on euthanized larvae, upon fixation in 4% paraformaldehyde (Sigma-Aldrich) and permeabilization in ice-cold acetone. Upon a 2-hour incubation in blocking solution [1% bovine serum albumin (BSA) + 5% donkey serum + 0.05% Triton X-100 in PBS), larvae were incubated overnight at 4°C with anti-human human lymphocyte antigen (HLA) (Abcam; 1:100 diluted). Larvae were then incubated overnight at 4°C with anti-rabbit immunoglobulin G (Alexa Fluor 647–conjugated, Jackson ImmunoResearch; 1:400 diluted) and 4′,6-diamidino-2-phenylindole (DAPI; Sigma-Aldrich; 1:1000 diluted). Xenografts were then postfixed and flat-mounted with lateral orientation in glycerol mounting medium. Z-stack images were acquired with a 25×/0.95 numerical aperture (NA) water immersion objective at 1-μm-z-stack interval on a Leica SP8 AOBS confocal microscope.

Primary tumor volume was measured in confocal z-stack immunofluorescence images, considering the sum of nuclear GFP and human HLA membrane signals, using a customized Fiji/ImageJ pipeline with Arivis Vision 4D 3.5.0 software. Volume was obtained by quantifying the area occupied by the primary tumor for each stack, computing the sum of all the areas, and multiplying by the z-step. All the analysis pipelines were optimized in collaboration with the Imaging Unit staff of the European Institute of Oncology (IEO).

Chemicals

LSD1i was administered at 2.5 μM over a period of 5 days, or as otherwise specified. Tg (1.5 μM; Merck Life Science, #T903) and TU (0.5 μg/ml; Merck Life Science, #T7765) were exploited as ER stressors, as indicated. TMZ (Sigma-Aldrich) was used at 50 μM at the time of cell plating over a period of 7 days. 2-DG (Sigma-Aldrich) was used at different concentrations (0, 0.1, 1, 2.5, and 5 mM).

Growth assay

To assess sensitivity to LSD1i, GBM TICs were cultured in 24-well plates at a density of 10^5 cells per well. Different concentrations of LSD1i (2.5, 5, and 10 mM) were assessed, and cells were counted after trypan blue staining at the indicated time points. This experiment was performed once with three replicates.

To evaluate sensitivity to TMZ, GBM TICs were cultured in 24-well plates at a density of 1×10^5 per well. After 7 days, cells were stained with trypan blue and counted. The experiment was conducted twice with three biological replicates. The excess over Bliss method has been applied to assess the presence of a synergistic or additive cooperation between LSD1i and TMZ treatments.

To evaluate the reliance on glycolysis, GBM TICs were cultured in 96-well plates at a density varying between 3×10^3 and 4.5×10^3 cells per well in 100 ml of medium. Varying concentrations of D-glucose (3, 1, and 0 g/liter) or 2-DG (5, 2.5, 1, 0.1, and 0 mM) were tested. Following 72 hours of culture, 100 ml of the CellTiter-Glo 3D (Promega) was added to each well. After a 25-min incubation at room temperature, the viability (luminescence) is measured with a PHERAstar FS plate reader (BMG Labtech) using 0.5 s per well of integration time.

Self-renewal assay

A total of 3×10^3 GBM TICs were seeded in a 35-mm culture plates in DMEM/F12 medium containing 50% of methylcellulose (MethoCult SF, STEMCELL Technology), with LSD1i or dimethyl sulfoxide as vehicle. Two weeks after plating, neurospheres were counted, collected, dissociated, and plated again.

Apoptosis

Caspase 3/7 activity was measured using Caspase-Glo assay kit (Promega), following the manufacturer's instruction. Briefly, GBM TICs were cultured in 96-well white opaque plates (Corning) at a density of 10^4 cells per well in 100 ml of medium containing LSD1i, Tg, or TU. After 24 hours for TU and Tg and 5 days for LSD1i, 100 μl of Caspase-Glo 3/7 assay reagent was added to each well, and the plate was placed on a shaker for ~30 s. After 30 min of room-temperature incubation in the dark, luminescence was read in a GloMax plate-reading luminometer (GloMax).

Immunofluorescence

A total of 10^5 GBM TICs were seeded on 13-mm Cell-Tak (Corning)–coated slides and fixed with 4% paraformaldehyde for 10 min at room temperature. For staining of MFN1 and MFN2 after 8 min of permeabilization in 0.1% Triton X-100 diluted into 0.1% BSA in PBS, coverslips were incubated with primary antibodies [MFN1 (1:50), Cell Signaling Technology, #14739S; MFN2 (1:100), Cell Signaling Technology, #11925S in 0.1% saponin in PBS) for 1 hour at room temperature. Coverslips were washed twice in PBS and incubated with a secondary antibody (ImmunoJackson Research; 1:200)

for 1 hour at room temperature, followed by a second wash in PBS and incubation with DAPI (Sigma-Aldrich; 1:1000 diluted) in PBS for 5 min. After postfixation for 2 min in 4% paraformaldehyde, coverslips were mounted with glycerol mounting medium. All images were obtained using a Leica TCS SP8 confocal microscope equipped with a HC PL APO 63×/1.4 oil immersion objective lens. To quantify mitofusin's signal intensity (raw integrated density per nucleus), the fluorescence intensity per field of view (FOV) was calculated using the "Measure" command on ImageJ and divided by the number of nuclei, which were manually counted, in the FOV according to the DAPI signal. The quantification of the raw integrated density per nucleus of each mitofusin after treatment compared to control condition is expressed as a percentage.

For staining of G3BP1, fixed cells were permeabilized with 0.1% Triton X-100 diluted into 0.1% BSA in PBS for 10 min and incubated with a blocking solution (5% BSA in PBS) for 1 hour at room temperature. Next, TICs were incubated with the primary antibody anti-G3BP1 (1:100; Proteintech, #13057-2-AP) diluted in 5% BSA in PBS overnight at 4°C. After washing three times with PBS, cells were incubated with anti-rabbit Alexa Fluor 488–coupled antibody (Thermo Fisher Scientific) for 1 hour at room temperature. Cells were then washed three times with PBS and incubated with iFluor555 phalloidin (Thermo Fisher Scientific, #A34055) for 1 hour at room temperature. Last, cells were incubated with DAPI (Sigma-Aldrich; 1:1000 diluted) in PBS for 5 min, washed with PBS for 2 min, and mounted in mowiol mounting medium [12% glycerol, 9.6% mowiol, and 1.5% DABCO in 0.1 M tris-HCl (pH 7.4)]. Confocal images were captured using the Eclipse Ti2 microscope (Nikon Europe B.V.) coupled with the X-Light V3 spinning disk (CrestOptics S.p.A), solid-state lasers from Lumencor CELESTA light engine, a multiband dichroic mirror, single-band emission filters, and a scientific complementary metal-oxide semiconductor (sCMOS) camera (Kinetix, Teledyne Photometrics). A total of 81 FOVs per sample were obtained with a PLAN APO λD 60×/1.42 oil immersion objective lens. Single optical sections of the DAPI, Alexa Fluor 488 (labeling G3BP1), and iFluor555 (labeling F-actin) signals were acquired at the middle plane of the nuclei.

To assess the mean intensity of the G3BP1 signal within the cells' cytoplasm, a custom Python-based image segmentation pipeline using the CellPose algorithm for cellular segmentation was used (*106*). This pipeline facilitated the identification of nuclear and cellular regions of interest using the DAPI and phalloidin signals.

All data analysis was conducted using RStudio software (version 2023.6.0.421, RStudio: Integrated Development for R, RStudio, Public Benefit Corporation, Boston, MA; www.rstudio.com/).

Representative super-resolution images of the same samples used to quantify the G3BP1 fluorescence were captured using the DeepSIM module (CrestOptics S.p.A., Rome, Italy) with a 100×/1.49 NA oil immersion objective lens (Nikon Europe B.V.) and the standard structured illumination mask (CrestOptics S.p.A.). The B/C settings of the super-resolution reconstructed images were maintained consistently for visualization purposes. These experiments were performed once for each TIC culture; total number of acquired cells are shown in figure legends.

Electron microscopy

Cell block preparation and EM analysis were performed according to standard protocol. Briefly, resin blocks of GBM TICs were sectioned using a Reichert Ultracut S and Leica EM UC7 ultramicrotome. Ultrathin sections (70 nm in thickness) were picked up on in-house formvar/carbon-coated grids and imaged on a Zeiss EM910 80-kV transmission EM (TEM) equipped with a 11M Quemesa charge-coupled device camera (EMSIS) and Tecnai 20 high-voltage EM operating at 200 kV.

For each condition, 20 micrographs corresponding to 20 TICs were recorded at a pixel size of 3.5 nm per pixel and were included in the analysis. MERC length was measured using the open-source software Fiji. The quantification method was adapted from Lam *et al.* (*107*). The experiment was performed twice for each TIC culture.

Mitochondrial structure

GBM TICs were incubated with MitoTracker Red (Thermo Fisher Scientific, #M7512) for 30 min at 37°C in a 5% CO_2-humidified incubator. After washing with PBS, cells were fixed with 4% paraformaldehyde for 8 min at room temperature, colored with DAPI, and mounted on 13-mm Cell-Tak (Corning)–coated slides. All images were obtained using a Leica TCS SP8 confocal microscope equipped with a HC PL APO 63×/1.4 oil immersion objective lens.

Mitochondrial branching analysis

Confocal images were captured using a Leica TCS SP8 scanning confocal microscope (Leica Microsystems GmbH) equipped with a 63×/1.4 oil immersion objective, resulting in a pixel size of 72 nm by 72 nm with a z-step of 300 nm or with an Eclipse Ti2 microscope (Nikon Europe B.V.), coupled with a Yokogawa CSU-W1 spinning disk system and a PLAN APO λ 100×/1.45 oil immersion objective lens, resulting in a pixel size of 68 nm by 68 nm with a z-step size of 200 nm. Scanning confocal images of mitochondrial fluorescence channel were deconvolved with Huygens Essential (version 19.04 Scientific Volume Imaging, The Netherlands; http://svi.nl).

Images obtained with the confocal spinning disk system were deconvolved using NIS-Elements software (v. 5.42.01). For each image, single cells' crops were extracted with a semiautomated, custom-made Fiji macro. Briefly, confocal stacks were projected with a max projection, and the DAPI channel was combined with the mitochondrial channel to identify the total area occupied by each cell. Images were then thresholded with a global thresholding method, and, when necessary, binary images were postprocessed with "fill holes" and "watershed" operation; areas containing a single cell were extracted from the FOV with the Analyze Particles command with the possibility to do manual corrections. Last, single-cell, 3D stack regions were extracted and saved for the following analysis steps. The extent of mitochondrial branching was extracted with another custom-made Fiji macro: Mitochondrial area was identified on the related fluorescence signal with the Auto Local Threshold Fiji's plugin using Bernsen method (for scanning confocal images) or with the Global Threshold Moments (for confocal spinning disk images), and binaries were then postprocessed with a Remove Outlier and a Skeletonize function; the Fiji's method Analyze Skeleton (2D/3D), which extracts the length of each segment (or branch) of the mitochondrial network, was applied.

Extracted results' tables were then exported and analyzed with RStudio (RStudio 2022.02.3 + 492 "Prairie Trillium" release). For each cell, the ratio between the number of branches and the number of skeletons was quantified.

ΔΨm and mass

Mitotracker orange (Thermo Fisher Scientific, #M7510) and mitotracker green (Thermo Fisher Scientific, #M7514) were used to measure ΔΨm and mass, respectively.

GBM TICs were incubated with these dyes for 30 min at 37°C with 5% CO_2-humidified incubator. Flow cytometry (BD FACSCelesta Cell Analyzer) was used to measure the mean fluorescence intensity. Data were analyzed using FlowJo software.

Oxygen consumption and extracellular flux analysis

Metabolic profiling was done using a Seahorse XF96 flux analyzer (Agilent Technologies). A total of 7×10^4 GBM TICs were resuspended in Seahorse XF DMEM (Agilent Technologies, #103680-100) supplemented with 1 mM pyruvate, 2 mM glutamine, and 10 mM glucose. Cells were then seeded on a 96-well Agilent Seahorse XF Cell Culture Microplate (Agilent Technologies) coated with polylysine (Merck Life Science, # P7405) and make them equilibrate for 1 hour at 37°C in non-CO_2 incubator. Last, cells were then centrifuged gently to adhere. The sensor cartridge was prepared by adding 1 μM oligomycin (O), 0.5 μM carbonyl cyanide *p*-trifluoromethoxyphenylhydrazone (FCCP), and 0.5 μM rotenone plus antimycin A (Rot/AA) for Seahorse XF Cell Mito Stress Test Kit (Agilent Technologies, #103015-100) and 0.5 μM Rot/AA and 50 mM 2-DG for Seahorse XF Glycolytic Rate Assay Kit (Agilent Technologies, #103344-100) to each cartridge port. O (1.5 μM) and Rot/AA (0.5 μM) were used for Seahorse XF Real-Time ATP Rate Assay Kit (Agilent Technologies, #103592-100). After measurement, cells were stained with crystal violet solution for 10 min, and the absorbance was measured at 540 nm following dissolution of the dye in a plate-reading spectrophotometer (GloMax). OCR and ECAR values were normalized on alive cells.

Redox ratio measurement

A total of 2×10^5 GBM TICs were seeded on Cell-Tak (Corning)–coated planar windows (Devotop Photonics). Label-free optical redox ratio measurements were taken with a laboratory-built nonlinear laser scanning microscope, as previously reported (*108*). Briefly, we used a dual-output laser source (FemtoFiber Pro, Toptica Photonics) to generate synchronized ≈1-ps duration pulses at 40-MHz repetition rate. The first output is a 780-nm pump beam. The second output is a Stokes beam, tuned at 1003 nm. We used a 100× 1.25 NA illumination objective (C-Apochromat, Carl Zeiss) and a 40× 1.30 NA collection objective (CFI Super Fluor, Nikon). The laser power was 7.5 and 0.5 mW for the pump and the Stokes beam, respectively. In the first scan, only the pump beam was used. The generated TPEF was detected in forward and in backward directions via two identical photomultiplier tubes: Backward-propagating fluorescence from nicotinamide adenine dinucleotide (phosphate) (reduced form) [NAD(P)H] + flavin adenine dinucleotide (FAD) was spectrally isolated using a 600-nm short-pass filter (Thorlabs); forward-propagating fluorescence from NAD(P)H was spectrally isolated using a 435/40-nm band-pass filter (Edmund Optics) (*109*). In the second scan, both beams were used. Continuous anti–Stokes Raman scattering (CARS) signal at the 2850 cm^{-1} Raman shift of lipids (*110*) was forward detected and spectrally isolated using a 650/40-nm band-pass filter (Thorlabs). Each image was obtained with a 1-ms pixel-dwell time and 200 pixels by 200 pixels for a 70 μm–by–70 μm area.

Image processing was performed in Phyton using SciKit and Scipy libraries. We applied a median filter and Otsu's thresholding on the CARS images to segment the cells from the substrate and create a cell mask. Each mask was visually inspected to check the quality of the segmentation. Single-cell segmentation was done using the watershed algorithm (*111*). For each cell, we identified the high-intensity pixels as the mitochondrial network and segmented it using a median filter and Yen's thresholding (*112*). We used this to measure the mean TPEF intensities of the mitochondrial areas and calculate the single-cells redox ratio as the NAD(P)H / [FAD + NAD(P)H] ratio.

We imaged 10 different culture plates for each TIC culture, equally divided into five control and five LSD1i-treated samples. Differences in the mitochondrial redox ratio between the LSD1i-treated and the vehicle groups were evaluated using the two-sided Mann-Whitney *U* test in Origin(Pro) (version 2022, OriginLab Corporation).

2-NBDG uptake

GBM TICs were incubated with 2-NBDG {2-[*N*-(7-nitrobenz-2-oxa-1,3-diazol-4-yl)amino]-2-deoxyglucose} (Thermo Fisher Scientific, #N13195) for 30 min at 37°C with 5% CO_2-humidified incubator. After washing cells, DAPI was used to discriminate alive cells. Flow cytometry (BD FACSCelesta Cell Analyzer) was used to measure the mean fluorescence intensity. Data were analyzed using FlowJo software.

Hexokinase activity assay

Hexokinase activity of GBM TICs (7.5×10^5 cells) was assessed using the Hexokinase Activity Assay Kit (Abcam, ab136957) following the manufacturer's instructions. Absorbances (optical density at 450 nm) were measured after an incubation time of 30 min in a plate-reading spectrophotometer (GloMax).

Measurements of Ca^{2+} concentration

A total of 2×10^5 GBM TICs were stained with Rhod-2AM (Thermo Fisher Scientific, #R1245MP) for 30 min at 37°C in a 5% CO_2-humidified incubator according to the manufacturer's protocol. After washing with PBS, nuclei were labeled with Hoechst 33342 (Thermo Fisher Scientific, #H3570), and images were acquired with a wide-field system (Thunder Imager, Leica Microsystems GmbH, Wetzlar Germany) equipped with fluorescence light-emitting diode (LED) illumination (Lumencor SpectraX, Beaverton, OR 97006, USA), a multiband dichroic mirror, different emission filters, an sCMOS camera (Leica, DFC9000 GTC), and a HC PL APO 60×/1.4 NA oil immersion objective lens. For each sample condition, 49 FOVs, randomly chosen, were acquired at a single focal plane. The bright-field (BF), Hoechst, and Rhod-2AM signals were acquired for each stage position. The Hoechst and BF signals were used to automatically segment the nuclei and the entire cells, respectively, by means of the Cellpose algorithm218 integrated in a custom-made Python script (Imaging Unit, IEO).

UPR reporter

UPR reporter activation was tested on a panel of four GBM-TICs with or without stress inducers, Tg and TU (300 to 3000 nM), and LSD1i (2.5 μM) for 24 hours. The cells were fixed and imaged using the Operetta High-Content Imaging platform. We used the confocal mode and a 20× water objective to image nine fields per well. LED power and detector exposure time were adjusted on vehicle-treated controls. The image analysis workflow involved filtering the mCherry channel to eliminate background, followed by identifying mCherry areas with stringent criteria to count only bright objects and remove cell debris. Object counting, area, and fluorescence intensity were measured, with mean, median, and sum of mCherry intensity calculated. Data analysis used mCherry sum intensities to provide a robust readout, compensating for dim intensities and amplifying differences between conditions with varying object counts and intensities. After importing raw data in R, drug concentrations and

metadata were merged, and *z*-scoring of the mCherry sum intensities was separately performed for each plate and subsequently merged back into a combined data frame. This approach effectively normalizes plate effects using positive and negative controls present on each plate. Mean *z*-scores for each compound were calculated from all replicate wells with $n = 3$ coming from nine fields per well each. Data were plotted as box plots with median (line inside the box), upper and lower quartiles (upper and lower boundaries of the box), and whiskers extending to the most extreme data points within 1.5 times the interquartile range from the upper and lower quartiles. Statistical significance was determined using pair-wise *t* test within the geom_signif () function in R.

Western blot

GBM TICs were lysed in RIPA (radioimmunoprecipitation assay) buffer [50 mM tris-HCl buffer (pH 8), 10 mM $CaCl_2$, 5 mM EGTA (pH 8), 250 mM NaCl, 10% glycerol, and 1% Triton X-100] supplemented with a cocktail of proteinase and phosphatase inhibitors [50 mM NAF, 10 mM NAPP, 10 mM NaOrtoV, phenylmethylsulfonyl fluoride (0.1 mg/ml), 10 μM leupeptin, and 10 μM aprotinin]. Protein lysates were centrifugated at 13,000 rpm for 30′ in a refrigerated centrifuge and then quantified with Bradford assay (Bio-Rad, #5000006) according to the manufacturer's protocol. Proteins were resolved by SDS–polyacrylamide gel electrophoresis, transferred to nitrocellulose membranes (Whatman Protran, Sigma-Aldrich), and blocked with 5% BSA in tris-buffered saline solution with Tween 20 (50 mM tris, 150 mM NaCl, and 0.1% Tween 20). Primary antibodies were incubated overnight at 4°C. Antibody binding was assessed by horseradish peroxidase–conjugated secondary antibody (Sigma-Aldrich; 1:5000 diluted). Images were acquired on a ChemiDoc XRS instrument (Bio-Rad). Primary antibodies used the following: anti-ATF4 (Cell Signaling Technology, #11815S; 1:500), anti–phospho-eIF2α (Cell Signaling Technology, #3398S; 1:1000), anti-eIF2α (Cell Signaling Technology, #5324S; 1:1000), anti-LSD1 (Cell Signaling Technology, #2139A; 1:1000), anti-LSD1 (Cell Signaling Technology, #2139A; 1:1000), anti-vinculin (Sigma-Aldrich, #V9131; 1:5000), anti-HKI (Cell Signaling Technology, #2024; 1:1000), anti-HKII (Cell Signaling Technology, #2867; 1:1000), anti-PKM2 (Cell Signaling Technology, #4053; 1:1000), anti-GAPDH (Cell Signaling Technology, #5174; 1:1000), anti-PFKP (Cell Signaling Technology, #8164; 1:1000), anti-LDHA (Cell Signaling Technology, #3582; 1:1000), anti–α-tubulin (Santa Cruz Biotechnology, #32293; 1:5000), and anti-PERK (Cell Signaling Technology, #3192S; 1:1000). Densitometric quantification of band intensity was performed using the Band Analysis tools of ImageLab software version 4.1 (Bio-Rad).

Liquid chromatography–mass spectrometry analysis

GBM TIC pellets were digested using the iST sample preparation kit (PreOmics), following the manufacturer's guidelines. Peptide mixtures were separated by reversed-phase chromatography on an EASY-Spray column (Thermo Fisher Scientific), 25 cm in length (inner diameter, 75 μm; PepMap C18, 2-μm particles), which was connected online to a Q Exactive Plus instrument (Thermo Fisher Scientific) through the EASY-Spray Ion Source (Thermo Fisher Scientific). Solvent A was 0.1% formic acid (FA) in double-distilled H_2O, and solvent B was 80% acetonitrile plus 0.1% FA. Peptides were injected in an aqueous 1% trifluoroacetic acid solution at a flow rate of 500 nl/min and were separated with 3 to 60% gradients (110 min, 3 to 21%; 18 min, 21 to 30%; 5 min, 30 to 60%) at a flow rate of 250 nl/min. The Q Exactive Plus instrument was operated in the data-dependent acquisition mode. Survey full-scan mass spectrometry (MS) spectra [mass/charge ratio (m/z) of 300 to 1650] were analyzed in the Orbitrap detector with a resolution of 70,000 at m/z 200. The 12 most intense peptide ions with charge states between 2 and 7 were sequentially isolated to an MS1 target value of 3×10^6 and fragmented by higher-energy collisional dissociation with a normalized collision energy setting of 28%. The maximum allowed ion accumulation times were 20 ms for full scans and 65 ms for MS/MS, and the target value for MS/MS was 1×10^5. The dynamic exclusion time was 20 s. The acquired raw data were analyzed using the integrated MaxQuant software v.1.6.2.3 (Max Planck Institute of Biochemistry) (*113*) and the Uniprot HUMAN (181029) databases. Enzyme specificity was set to trypsin, and two missed cleavages were allowed. Methionine oxidation and N-terminal acetylation were included as variable modifications and the false discovery rate (FDR) was set to 1%, both at the protein and peptide level. The label-free software MaxLFQ (*114*) was activated, with the "match between runs" feature (match from and to, matching time window = 2 min).

Data analysis was performed with Perseus software. The protein group output table from MaxQuant was filtered for "reverse," "only identified by site," "contaminants," and at 3 or 70% of valid values in each group. Missing values were then imputed by random numbers drown from a normal distribution, assuming that these values belonged to low-intensity spectrum of the distribution (down shift = 1.8 and width = 0.3). To determine significantly changing proteins between conditions, a two-sample Student's *t* test was used, with a $P = 0.01$. Pathway analyses of the proteins significantly changing in the comparison between $LSD1i^{Sens}$ and $LSD1i^{Res}$ TICs was carried out using Reactome (https://reactome.org/).

In vitro synthetic lethal shRNA screening

The human metabolic shRNA library (Cellecta) (gift from L. Lanfrancone, IEO, Milan) is engineered into the pRSI17-U6-(sh)-UbiC-GFP-2A-Puro lentiviral vector containing the puromycin resistance and the GFP marker. It contains 2924 lentiviral vectors, targeting 297 genes with each shRNA (10 different shRNA constructs per gene) univocally associated with a barcode cassette of 18 degenerated, nonoverlapping nucleotides. Genes targeted by the shRNA constructs are listed in table S2. 293T cells were transfected with Lipofectamine LTX and PLUS Reagent Kit (Invitrogen, #15338100). Transfection was performed in 15-cm tissue-cultured plates according to the manufacturer's indications. Briefly, for each transfection were used 6 μg of DNA library, 7 μg of pMD2G–vesicular stomatitis virus glycoprotein, and 24 μg of pCMV-DR8.2. After 24 hours, the transfection medium was replaced with complete culture medium, and viral supernatants were collected at 24 and 48 hours, filtered through 0.45-μm filters, ultracentrifugated at 22,000 rpm for 2 hours to be ultimately resuspended in sterile PBS. Concentrated virus was stored at −80°C. $LSD1i^{Res}$ GBM#23 cells were infected with a low multiplicity of infection equal to 0.2 and at a high library coverage (500×). Infected cells were selected with puromycin and randomized in three branches with two technical replicates per condition: vehicle, 2.5 μM LSD1i, and 5 μM LSD1i. A reference condition was collected straight after puromycin selection to retrieve the initial relative abundance of each shRNA construct at time zero. Cells were kept in culture up to 6 weeks and split once a week. LSD1i was refreshed at every splitting. Genomic DNA was isolated from 6-week time point, and shRNA relative abundance was retrieved by a two-step polymerase chain

reaction (PCR) amplification procedure, followed by next-generation sequencing (NGS) reaction. A PCR1 reaction was used to amplify the shRNA-specific barcode sequence and used as template for PCR2 reaction to add specific indexes and adaptors to each sample. Integrity and quantification of PCR purified products were assessed with Bioanalyzer 2000 (Agilent) before proceeding with NGS (Illumina NovaSeq 6000) with the following parameters: paired-end sequencing, read length of 50 base pairs, sequencing depth of 30 million reads per sample. Barcodes and corresponding shRNAs were then identified by aligning sequencing output to the sequences of the metabolic library barcodes. The matched reads were counted, normalized, and then used for analysis. Candidate genes to be potential synthetic lethal with LSD1i were identified if they satisfied the following criteria: (i) the median of Δfold change (FC) for all the shRNAs specific for the gene < 0 [ΔFC LSD1i = ($\log_2$ LSD1i) − ($\log_2$ vehicle) < 0]; (ii) >3 shRNAs specific for the gene showing ΔFC < −1; (iii) shRNAs specific for the gene not being counterselected in vehicle experimental arm [≥5 shRNA $\log_2$ FC vehicle (vehicle/reference after puromycin) > 0].

GBM TIC infection

LSD1 silencing was achieved using MISSION pLKO.1-puro empty vector plasmid DNA (Sigma-Aldrich) harboring either the sequence targeting human LSD1 (TRCN0000046071, sh#71) or a nontargeting shRNA (SHC002, shNT) used as a control, as previously described (*21*). Tet-Off-H2B-GFP lentiviral vector (gift from P. G. Pelicci, IEO, Milan) was exploited as a nuclear tag for the identification of TICs transplanted in embryonic zebrafish for tumor volume quantification. pLentiLox3.7 vector encoding Luc2 cDNA (gift from L. Lanfrancone, IEO, Milan) was used to generate GBM TICs expressing firefly luciferase for monitoring tumor growth in vivo (*21*). Lentivector for PGAP1 cDNA overexpression (catalog no. RC213837L4) and the corresponding empty vector (catalog no. PS100093) were commercially purchased from OriGene.

The UPRE reporter (*52*) modified with XBP1 sequence [gift from G. Gargiulo, Max Delbrück Center (MDC), Berlin] was exploited to measure IRE1α-XBP1 pathway activation in GBM TICs treated with Tg, TU, and LSD1i.

shRNA oligonucleotides targeting human PGAP1 mRNA were cloned into pRSI17-U6-(sh)-UbiC-GFP-2A-Puro linearized vector according to the manufacturer's instructions (Cellecta; sh#1, 5′-ACCGGCTAAATGCTCGACACATAAATGTTAATATTCATAG-CATTTATGTGTCGAGCATTTAGTTTT-3′; sh#3, 5′- ACCGGCAT GCCCACAATCTATATTATGTTAATATTCATAGCATAATATAG-ATTGTGGGCATGTTTT-3′). A lentiviral plasmid expressing a scrambled shRNA was used as control (5′-ACCGGATATCTCGCAA TGTTGGTGTTGTTAATATTCATAGCAACACCAACATT-GCGAGATATTTTT-3′). sh#57 was purchased from Sigma-Aldrich (TRCN0000047157). Lentivirus production and GBM TIC transduction were performed as previously described (*21*).

RNA extraction and real-time quantitative PCR

RNA was isolated from GBM TICs using Quick-RNA Miniprep Kit (Zymo Research, #R1054) following the manufacturer's specifications. cDNA was synthesized with high-capacity cDNA reverse transcription kit (Thermo Fisher Scientific). Real-time quantitative PCR was performed by Viia7 Real-Time PCR system (Thermo Fisher Scientific) using Fast SYBR Green (Applied Biosystems) according to standard protocols. Threshold cycle (C_t) values for each gene were normalized to housekeeping genes expression level. The primers used are listed in table S3.

Library preparation, RNA sequencing, gene set enrichment analysis, and in silico analysis

Libraries were prepared using the TruSeq Stranded Total RNA Kit (Illumina, #20020598) according to the manufacturer's instructions. Libraries were multiplexed, clustered, and sequenced on an Illumina NovaSeq 6000. RNA sequencing (RNA-seq) fastq files were processed using RSEM v 1.3.1 (*115*). Reads were aligned to the human genome version hg38. Gene annotations were downloaded from Ensembl GRCh38/hg38 v100. Corresponding gct matrix file was used as input for gene set enrichment analysis (GSEA) 4.3.2 to perform a set of functional enrichment analyses of LSD1i versus vehicle cells with respect to Human MitoCarta3.0 gene sets (*42*) selecting a custom list of significantly enriched terms among the ones reporting |NES| > 1 (where NES is normalized enrichment score) and FDR < 0.05.

mRNA-seq expression data for LSD1i^{Sens} and LSD1i^{Res} TICs were obtained from Lazzarini *et al.* (*116*). LSD1i^{Sens} versus LSD1i^{Res} TICs were also analyzed using GSEA 4.3.2 performing a functional enrichment analysis with respect to set Hallmark gene sets from the MSigDB selecting a custom list of significantly enriched terms among the ones reporting |NES| > 1 and FDR < 0.05. Moreover, a similar GSEA analysis was used to compare LSD1iSens and LSD1i^{Res} TICs using a custom GSEA reference dataset built from the molecular signatures published by Garofano and colleagues (*5*) in table S6J (GBM MTC, NEU, and PPR signatures).

cBioPortal (*117*) was used to download GBM samples from the TCGA Firehorse Legacy dataset, selecting only samples characterized by a PGAP1 expression level of |*z*-score| > 1.2 based on the log RNA-seq V2 RSEM pipeline of analysis. Samples were subsequently divided, on the basis of the score expression value of PGAP1, into two sets: PGAP1^{Low} and PGAP1^{High} samples. PGAP1^{Low} and PGAP1^{High} samples underwent a GSEA functional annotation analysis based on Hallmark gene sets from the MSigDB with GSEA 4.3.2, selecting a subset of Hallmark gene sets reporting |NES| > 1 and FDR < 0.05.

For all GSEA, permutation type was set on gene sets. Dot plot reporting selectively enriched terms were produced using "ggplot2" library in R (https://ggplot2.tidyverse.org).

PGAP1 expression level from GBM tissues and normal brain samples were downloaded from GEPIA2 website (http://gepia2.cancer-pku.cn/#index) (*118*).

Statistical analysis

All experiments were performed at least three times with a minimum of three independent replicates, unless otherwise specified. Data were statistically analyzed by unpaired Student's *t* test, or Mann-Whitney *U* test, or one-way analysis of variance (ANOVA) with Kruskal-Wallis correction using GraphPad Prism, as described in figure legends. Kaplan-Meier curves were generated by GraphPad Prism, and log-rank test was used to assess the significance of survival outcomes.

Mixed effect model was applied considering group and treatment as categorical variables and time as fixed effect. Basal values were also included as covariate. Interaction (group*treatment) was also considered in the analyses. Outcome changes over time were evaluated, and stratified group analyses were performed to assess differences between treatments. Logarithmic transformation was applied to reach normal distribution of residuals. All statistical tests

were two sided, and results with $P < 0.05$ were considered statistically significant. Statistical analyses were performed using the R statistical software (version 4.2.3).

For the experiment shown in Fig. 7C, selected lists of enriched Hallmark gene sets from the GSEA results from patients with $PGAP1^{Low}$ versus $PGAP1^{High}$ and LSD1i-sensitive versus LSD1i-resistant TICs were compared using the implementation of the hypergeometric test "phyper" in R. The hypergeometric P values were corrected using Benjamini-Hochberg correction. Corrected hypergeometric P values ($-\log_{10}$) are reported as bar plots. Only a selection of tested hallmarks is reported.

The correlation analysis between the expression of LSD1 and the pathways of glycolysis and OXPHOS was conducted as follows. First, the Gliovis database (*43*) was interrogated to extract Spearman correlation values between the expression level of LSD1 and all genes in the human genome, using the CGGA and Gravendeel datasets. Only samples with tumor type "primary" and subtype defined as "all" were used. We then selected gene pairs associated with |correlation index| > 0.3 and an adjusted $P < 0.05$. Subsequently, complete gene sets for glycolysis and OXPHOS were retrieved from the Kyoto Encyclopedia of Genes and Genomes database (*119*), for a total of 67 glycolysis-related genes and 135 genes related to OXPHOS. Last, correlation plots were generated using the "corrplot" package in R, displaying only the intersections among the genes belonging to the selected pathways and characterized by significant correlations with LSD1.

All data are represented as mean and SD or SEM and described in the figure legends. Statistical significance was defined as $*P < 0.05$; $**P < 0.01$; $***P < 0.001$.

Supplementary Materials

The PDF file includes:
Figs. S1 to S6
Tables S1 and S3
Legend for table S2

Other Supplementary Material for this manuscript includes the following:
Table S2

REFERENCES AND NOTES

1. D. N. Louis, A. Perry, P. Wesseling, D. J. Brat, I. A. Cree, D. Figarella-Branger, C. Hawkins, H. K. Ng, S. M. Pfister, G. Reifenberger, R. Soffietti, A. von Deimling, D. W. Ellison, The 2021 WHO classification of tumors of the central nervous system: A summary. *Neuro Oncol.* **23**, 1231–1251 (2021).
2. R. Stupp, M. E. Hegi, W. P. Mason, M. J. van den Bent, M. J. Taphoorn, R. C. Janzer, S. K. Ludwin, A. Allgeier, B. Fisher, K. Belanger, P. Hau, A. A. Brandes, J. Gijtenbeek, C. Marosi, C. J. Vecht, K. Mokhtari, P. Wesseling, S. Villa, E. Eisenhauer, T. Gorlia, M. Weller, D. Lacombe, J. G. Cairncross, R.-O. Mirimanoff, European Organisation for Research and Treatment of Cancer Brain Tumour and Radiation Oncology Groups, Effects of radiotherapy with concomitant and adjuvant temozolomide versus radiotherapy alone on survival in glioblastoma in a randomised phase III study: 5-year analysis of the EORTC-NCIC trial. *Lancet Oncol.* **10**, 459–466 (2009).
3. B. C. Prager, S. Bhargava, V. Mahadev, C. G. Hubert, J. N. Rich, Glioblastoma stem cells: Driving resilience through chaos. *Trends Cancer* **6**, 223–235 (2020).
4. C. Neftel, J. Laffy, M. G. Filbin, T. Hara, M. E. Shore, G. J. Rahme, A. R. Richman, D. Silverbush, M. L. Shaw, C. M. Hebert, J. Dewitt, S. Gritsch, E. M. Perez, L. N. Gonzalez Castro, X. Lan, N. Druck, C. Rodman, D. Dionne, A. Kaplan, M. S. Bertalan, J. Small, K. Pelton, S. Becker, D. Bonal, Q.-D. Nguyen, R. L. Servis, J. M. Fung, R. Mylvaganam, L. Mayr, J. Gojo, C. Haberler, R. Geyeregger, T. Czech, I. Slavc, B. V. Nahed, W. T. Curry, B. S. Carter, H. Wakimoto, P. K. Brastianos, T. T. Batchelor, A. Stemmer-Rachamimov, M. Martinez-Lage, M. P. Frosch, I. Stamenkovic, N. Riggi, E. Rheinbay, M. Monje, O. Rozenblatt-Rosen, D. P. Cahill, A. P. Patel, T. Hunter, I. M. Verma, K. L. Ligon, D. N. Louis, A. Regev, B. E. Bernstein, I. Tirosh, M. L. Suvà, An integrative model of cellular states, plasticity, and genetics for glioblastoma. *Cell* **178**, 835–849.e21 (2019).
5. L. Garofano, S. Migliozzi, Y. T. Oh, F. D'Angelo, R. D. Najac, A. Ko, B. Frangaj, F. P. Caruso, K. Yu, J. Yuan, W. Zhao, A. Luisa Di Stefano, F. Bielle, T. Jiang, P. Sims, M. L. Suvà, F. Tang, X.-D. Su, M. Ceccarelli, M. Sanson, A. Lasorella, A. Iavarone, Pathway-based classification of glioblastoma uncovers a mitochondrial subtype with therapeutic vulnerabilities. *Nat. Cancer* **2**, 141–156 (2021).
6. M. J. Schmitt, C. Company, Y. Dramaretska, I. Barozzi, A. Göhrig, S. Kertalli, M. Großmann, H. Naumann, M. P. Sanchez-Bailon, D. Hulsman, R. Glass, M. Squatrito, M. Serresi, G. Gargiulo, Phenotypic mapping of pathologic cross-talk between glioblastoma and innate immune cells by synthetic genetic tracing. *Cancer Discov.* **11**, 754–777 (2021).
7. L. M. Richards, O. K. N. Whitley, G. MacLeod, F. M. G. Cavalli, F. J. Coutinho, J. E. Jaramillo, N. Svergun, M. Riverin, D. C. Croucher, M. Kushida, K. Yu, P. Guilhamon, N. Rastegar, M. Ahmadi, J. K. Bhatti, D. A. Bozek, N. Li, L. Lee, C. Che, E. Luis, N. I. Park, Z. Xu, T. Ketela, R. A. Moore, M. A. Marra, J. Spears, M. D. Cusimano, S. Das, M. Bernstein, B. Haibe-Kains, M. Lupien, H. A. Luchman, S. Weiss, S. Angers, P. B. Dirks, G. D. Bader, T. J. Pugh, Gradient of developmental and injury response transcriptional states defines functional vulnerabilities underpinning glioblastoma heterogeneity. *Nat. Cancer* **2**, 157–173 (2021).
8. Q. Wang, B. Hu, X. Hu, H. Kim, M. Squatrito, L. Scarpace, A. C. DeCarvalho, S. Lyu, P. Li, Y. Li, F. Barthel, H. J. Cho, Y.-H. Lin, N. Satani, E. Martinez-Ledesma, S. Zheng, E. Chang, C.-E. G. Sauvé, A. Olar, Z. D. Lan, G. Finocchiaro, J. J. Phillips, M. S. Berger, K. R. Gabrusiewicz, G. Wang, E. Eskilsson, J. Hu, T. Mikkelsen, R. A. DePinho, F. Muller, A. B. Heimberger, E. P. Sulman, D.-H. Nam, R. G. W. Verhaak, Tumor evolution of glioma-intrinsic gene expression subtypes associates with immunological changes in the microenvironment. *Cancer Cell* **32**, 42–56.e6 (2017).
9. I. Saga, S. Shibao, J. Okubo, S. Osuka, Y. Kobayashi, S. Yamada, S. Fujita, K. Urakami, M. Kusuhara, K. Yoshida, H. Saya, O. Sampetrean, Integrated analysis identifies different metabolic signatures for tumor-initiating cells in a murine glioblastoma model. *Neuro Oncol.* **16**, 1048–1056 (2014).
10. E. I. Spehalski, J. A. Lee, C. Peters, P. Tofilon, K. Camphausen, The quiescent metabolic phenotype of glioma stem cells. *J. Proteomics Bioinform.* **12**, 96–103 (2019).
11. S. Oudard, F. Arvelo, L. Miccoli, F. Apiou, A. Dutrillaux, M. Poisson, B. Dutrillaux, M. Poupon, High glycolysis in gliomas despite low hexokinase transcription and activity correlated to chromosome 10 loss. *Br. J. Cancer* **74**, 839–845 (1996).
12. S. Shibao, N. Minami, N. Koike, N. Fukui, K. Yoshida, H. Saya, O. Sampetrean, Metabolic heterogeneity and plasticity of glioma stem cells in a mouse glioblastoma model. *Neuro Oncol.* **20**, 343–354 (2018).
13. K. Oizel, C. Chauvin, L. Oliver, C. Gratas, F. Geraldo, U. Jarry, E. Scotet, M. Rabe, M.-C. Alves-Guerra, R. Teusan, F. Gautier, D. Loussouarn, V. Compan, J.-C. Martinou, F. M. Vallette, C. Pecqueur, Efficient mitochondrial glutamine targeting prevails over glioblastoma metabolic plasticity. *Clin. Cancer Res.* **23**, 6292–6304 (2017).
14. F. Puca, F. Yu, C. Bartolacci, P. Pettazzoni, A. Carugo, E. Huang-Hobbs, J. Liu, C. Zanca, F. Carbone, E. Del Poggetto, J. Gumin, P. Dasgupta, S. Seth, S. Srinivasan, F. F. Lang, E. P. Sulman, P. L. Lorenzi, L. Tan, M. Shan, Z. P. Tolstyka, M. Kachman, L. Zhang, S. Gao, A. K. Deem, G. Genovese, P. P. Scaglioni, C. A. Lyssiotis, A. Viale, G. F. Draetta, Medium-chain acyl-CoA dehydrogenase protects mitochondria from lipid peroxidation in glioblastoma. *Cancer Discov.* **11**, 2904–2923 (2021).
15. C. Chen, Z. Zhang, C. Liu, B. Wang, P. Liu, S. Fang, F. Yang, Y. You, X. Li, ATF4-dependent fructolysis fuels growth of glioblastoma multiforme. *Nat. Commun.* **13**, 6108 (2022).
16. F. Torrisi, S. D'Aprile, S. Denaro, A. M. Pavone, C. Alberghina, A. Zappalà, R. Giuffrida, L. Salvatorelli, G. Broggi, G. G. Magro, V. Calabrese, N. Vicario, R. Parenti, Epigenetics and metabolism reprogramming interplay into glioblastoma: Novel insights on immunosuppressive mechanisms. *Antioxidants* **12**, 220 (2023).
17. A. V. Krauze, S. D. Myrehaug, M. G. Chang, D. J. Holdford, S. Smith, J. Shih, P. J. Tofilon, H. A. Fine, K. Camphausen, A phase 2 study of concurrent radiation therapy, temozolomide, and the histone deacetylase inhibitor valproic acid for patients with glioblastoma. *Int. J. Radiat. Oncol. Biol. Phys.* **92**, 986–992 (2015).
18. M. Vieito, M. Simonelli, F. de Vos, V. Moreno, M. Geurts, E. Lorenzi, M. Macchini, M. J. van den Bent, G. Del Conte, M. de Jonge, M. C. Martín-Soberón, B. Amoroso, T. Sanchez-Perez, M. Zuraek, B. Hanna, I. Aronchik, E. Filvaroff, H. Chang, C. Mendez, M. Arias Parro, X. Wei, Z. Nikolova, J. M. Sepulveda, Trotabresib (CC-90010) in combination with adjuvant temozolomide or concomitant temozolomide plus radiotherapy in patients with newly diagnosed glioblastoma. *Neuro. Oncol. Adv.* **4**, vdac146 (2022).
19. K. B. Peters, E. S. Lipp, E. Miller, J. E. Herndon, F. McSherry, A. Desjardins, D. A. Reardon, H. S. Friedman, Phase I/II trial of vorinostat, bevacizumab, and daily temozolomide for recurrent malignant gliomas. *J. Neurooncol.* **137**, 349–356 (2018).
20. P. Vianello, O. A. Botrugno, A. Cappa, R. Dal Zuffo, P. Dessanti, A. Mai, B. Marrocco, A. Mattevi, G. Meroni, S. Minucci, G. Stazi, F. Thaler, P. Trifiró, S. Valente, M. Villa, M. Varasi, C. Mercurio, Discovery of a novel inhibitor of histone lysine-specific demethylase 1A (KDM1A/LSD1) as orally active antitumor agent. *J. Med. Chem.* **59**, 1501–1517 (2016).

21. S. Faletti, D. Osti, E. Ceccacci, C. Richichi, B. Costanza, L. Nicosia, R. Noberini, G. Marotta, L. Furia, M. R. Faretta, S. Brambillasca, M. Quarto, L. Bertero, R. Boldorini, B. Pollo, S. Gandini, D. Cora, S. Minucci, C. Mercurio, M. Varasi, T. Bonaldi, G. Pelicci, LSD1-directed therapy affects glioblastoma tumorigenicity by deregulating the protective ATF4-dependent integrated stress response. *Sci. Transl. Med.* **13**, eabf7036 (2021).
22. A. Sakamoto, S. Hino, K. Nagaoka, K. Anan, R. Takase, H. Matsumori, H. Ojima, Y. Kanai, K. Arita, M. Nakao, Lysine demethylase LSD1 coordinates glycolytic and mitochondrial metabolism in hepatocellular carcinoma cells. *Cancer Res.* **75**, 1445–1456 (2015).
23. D. Wang, C.-D. Liu, M.-L. Tian, C.-Q. Tan, G. Shu, Q.-Y. Jiang, L. Zhang, Y.-L. Yin, Propionate promotes intestinal lipolysis and metabolic benefits via AMPK/LSD1 pathway in mice. *J. Endocrinol.* **243**, 187–197 (2019).
24. Y. Cao, L. Tang, K. Du, K. Paraiso, Q. Sun, Z. Liu, X. Ye, Y. Fang, F. Yuan, H. Chen, Y. Chen, X. Wang, C. Yu, I. L. Blitz, P. H. Wang, L. Huang, H. Cheng, X. Lu, K. W. Y. Cho, M. Seldin, Z. Fang, Q. Yang, Anterograde regulation of mitochondrial genes and FGF21 signaling by hepatic LSD1. *JCI Insight* **6**, e147692 (2021).
25. D. Duteil, E. Metzger, D. Willmann, P. Karagianni, N. Friedrichs, H. Greschik, T. Günther, R. Buettner, I. Talianidis, D. Metzger, R. Schüle, LSD1 promotes oxidative metabolism of white adipose tissue. *Nat. Commun.* **5**, 4093 (2014).
26. D. Duteil, M. Tosic, F. Lausecker, H. Z. Nenseth, J. M. Müller, S. Urban, D. Willmann, K. Petroll, N. Messaddeq, L. Arrigoni, T. Manke, J.-W. Kornfeld, J. C. Brüning, V. Zagoriy, M. Meret, J. Dengjel, T. Kanouni, R. Schüle, Lsd1 ablation triggers metabolic reprogramming of brown adipose tissue. *Cell Rep.* **17**, 1008–1021 (2016).
27. K. Anan, S. Hino, N. Shimizu, A. Sakamoto, K. Nagaoka, R. Takase, K. Kohrogi, H. Araki, Y. Hino, S. Usuki, S. Oki, H. Tanaka, K. Nakamura, F. Endo, M. Nakao, LSD1 mediates metabolic reprogramming by glucocorticoids during myogenic differentiation. *Nucleic Acids Res.* **46**, 5441–5454 (2018).
28. O. M. Eichhoff, C. I. Stoffel, J. Käsler, L. Briker, P. Turko, G. Karsai, N. Zila, V. Paulitschke, P. F. Cheng, A. Leitner, A. Bileck, N. Zamboni, A. Irmisch, Z. Balazs, A. Tastanova, S. Pascoal, P. Johansen, R. Wegmann, J. Mena, A. Othman, V. S. Viswanathan, J. Wenzina, A. Aloia, A. Saltari, A. Dzung, M. Krauthammer, S. L. Schreiber, T. Hornemann, M. Distel, B. Snijder, R. Dummer, M. P. Levesque, ROS induction targets persister cancer cells with low metabolic activity in NRAS-mutated melanoma. *Cancer Res.* **83**, 1128–1146 (2023).
29. K. Pakos-Zebrucka, I. Koryga, K. Mnich, M. Ljujic, A. Samali, A. M. Gorman, The integrated stress response. *EMBO Rep.* **17**, 1374–1395 (2016).
30. P. Klein, S. M. Kallenberger, H. Roth, K. Roth, T. B. N. Ly-Hartig, V. Magg, J. Aleš, S. R. Talemi, Y. Qiang, S. Wolf, O. Oleksiuk, R. Kurilov, B. Di Ventura, R. Bartenschlager, R. Eils, K. Rohr, F. A. Hamprecht, T. Höfer, O. T. Fackler, G. Stoecklin, A. Ruggieri, Temporal control of the integrated stress response by a stochastic molecular switch. *Sci. Adv.* **8**, eabk2022 (2022).
31. M. Magarin, T. Pohl, A. Lill, H. Schulz, F. Blaschke, A. Heuser, L. Thierfelder, S. Donath, J.-D. Drenckhahn, Embryonic cardiomyocytes can orchestrate various cell protective mechanisms to survive mitochondrial stress. *J. Mol. Cell. Cardiol.* **97**, 1–14 (2016).
32. X. R. Bao, S.-E. Ong, O. Goldberger, J. Peng, R. Sharma, D. A. Thompson, S. B. Vafai, A. G. Cox, E. Marutani, F. Ichinose, W. Goessling, A. Regev, S. A. Carr, C. B. Clish, V. K. Mootha, Mitochondrial dysfunction remodels one-carbon metabolism in human cells. *eLife* **5**, e10575 (2016).
33. N. A. Khan, J. Nikkanen, S. Yatsuga, C. Jackson, L. Wang, S. Pradhan, R. Kivelä, A. Pessia, V. Velagapudi, A. Suomalainen, mTORC1 regulates mitochondrial integrated stress response and mitochondrial myopathy progression. *Cell Metab.* **26**, 419–428.e5 (2017).
34. P. M. Quirós, M. A. Prado, N. Zamboni, D. D'Amico, R. W. Williams, D. Finley, S. P. Gygi, J. Auwerx, Multi-omics analysis identifies ATF4 as a key regulator of the mitochondrial stress response in mammals. *J. Cell Biol.* **216**, 2027–2045 (2017).
35. Y. Miyazono, S. Hirashima, N. Ishihara, J. Kusukawa, K. Nakamura, K. Ohta, Uncoupled mitochondria quickly shorten along their long axis to form indented spheroids, instead of rings, in a fission-independent manner. *Sci. Rep.* **8**, 350 (2018).
36. T. Ahmad, K. Aggarwal, B. Pattnaik, S. Mukherjee, T. Sethi, B. K. Tiwari, M. Kumar, A. Micheal, U. Mabalirajan, B. Ghosh, S. Sinha Roy, A. Agrawal, Computational classification of mitochondrial shapes reflects stress and redox state. *Cell Death Dis.* **4**, e461 (2013).
37. T. F. Sergeeva, M. V. Shirmanova, O. A. Zlobovskaya, A. I. Gavrina, V. V. Dudenkova, M. M. Lukina, K. A. Lukyanov, E. V. Zagaynova, Relationship between intracellular pH, metabolic co-factors and caspase-3 activation in cancer cells during apoptosis. *Biochim. Biophys. Acta Mol. Cell Res.* **1864**, 604–611 (2017).
38. S. Paglin, N.-Y. Lee, C. Nakar, M. Fitzgerald, J. Plotkin, B. Deuel, N. Hackett, M. McMahill, E. Sphicas, N. Lampen, J. Yahalom, Rapamycin-sensitive pathway regulates mitochondrial membrane potential, autophagy, and survival in irradiated MCF-7 cells. *Cancer Res.* **65**, 11061–11070 (2005).
39. S. Kaspar, C. Oertlin, K. Szczepanowska, A. Kukat, K. Senft, C. Lucas, S. Brodesser, M. Hatzoglou, O. Larsson, I. Topisirovic, A. Trifunovic, Adaptation to mitochondrial stress requires CHOP-directed tuning of ISR. *Sci. Adv.* **7**, eabf0971 (2021).
40. C. M. Gonçalves de Faria, H. Ciol, V. Salvador Bagnato, S. Pratavieira, Effects of photobiomodulation on the redox state of healthy and cancer cells. *Biomed. Opt. Express* **12**, 3902–3916 (2021).
41. A. Podsednik, A. Jacob, L. Z. Li, H. N. Xu, Relationship between optical redox status and reactive oxygen species in cancer cells. *React. Oxyg. Species* **9**, 95–108 (2020).
42. S. Rath, R. Sharma, R. Gupta, T. Ast, C. Chan, T. J. Durham, R. P. Goodman, Z. Grabarek, M. E. Haas, W. H. W. Hung, P. R. Joshi, A. A. Jourdain, S. H. Kim, A. V. Kotrys, S. S. Lam, J. G. McCoy, J. D. Meisel, M. Miranda, A. Panda, A. Patgiri, R. Rogers, S. Sadre, H. Shah, O. S. Skinner, T.-L. To, M. A. Walker, H. Wang, P. S. Ward, J. Wengrod, C.-C. Yuan, S. E. Calvo, V. K. Mootha, MitoCarta3.0: An updated mitochondrial proteome now with sub-organelle localization and pathway annotations. *Nucleic Acids Res.* **49**, D1541–D1547 (2021).
43. R. L. Bowman, Q. Wang, A. Carro, R. G. W. Verhaak, M. Squatrito, GlioVis data portal for visualization and analysis of brain tumor expression datasets. *Neuro Oncol.* **19**, 139–141 (2017).
44. R. Bravo, J. M. Vicencio, V. Parra, R. Troncoso, J. P. Munoz, M. Bui, C. Quiroga, A. E. Rodriguez, H. E. Verdejo, J. Ferreira, M. Iglewski, M. Chiong, T. Simmen, A. Zorzano, J. A. Hill, B. A. Rothermel, G. Szabadkai, S. Lavandero, Increased ER–mitochondrial coupling promotes mitochondrial respiration and bioenergetics during early phases of ER stress. *J. Cell Sci.* **124**, 2143–2152 (2011).
45. C. Lopez-Crisosto, A. Díaz-Vegas, P. F. Castro, B. A. Rothermel, R. Bravo-Sagua, S. Lavandero, Endoplasmic reticulum–mitochondria coupling increases during doxycycline-induced mitochondrial stress in HeLa cells. *Cell Death Dis.* **12**, 657 (2021).
46. Z. Ma, C. Fan, Y. Yang, S. Di, W. Hu, T. Li, Y. Zhu, J. Han, Z. Xin, G. Wu, J. Zhao, X. Li, X. Yan, Thapsigargin sensitizes human esophageal cancer to TRAIL-induced apoptosis via AMPK activation. *Sci. Rep.* **6**, 35196 (2016).
47. E. Almstedt, E. Rosén, M. Gloger, R. Stockgard, N. Hekmati, K. Koltowska, C. Krona, S. Nelander, Real-time evaluation of glioblastoma growth in patient-specific zebrafish xenografts. *Neuro Oncol.* **24**, 726–738 (2022).
48. E. W. Newcomb, D. Zagzag, "The murine GL261 glioma experimental model to assess novel brain tumor treatments" in *CNS Cancer* (Humana Press, 2009), pp. 227–241; http://link.springer.com/10.1007/978-1-60327-553-8_12 .
49. J. Kim, K.-L. Guan, mTOR as a central hub of nutrient signalling and cell growth. *Nat. Cell Biol.* **21**, 63–71 (2019).
50. M. Oshi, A. M. Roy, L. Yan, M. Sasamoto, Y. Tokumaru, R. Wu, A. Yamada, S. Yamamoto, T. Chishima, K. Narui, I. Endo, K. Takabe, Accelerated glycolysis in tumor microenvironment is associated with worse survival in triple-negative but not consistently with ER+/HER2- breast cancer. *Am. J. Cancer Res.* **13**, 3041–3054 (2023).
51. D. Zhong, X. Liu, K. Schafer-Hales, A. I. Marcus, F. R. Khuri, S.-Y. Sun, W. Zhou, 2-Deoxyglucose induces Akt phosphorylation via a mechanism independent of LKB1/AMP-activated protein kinase signaling activation or glycolysis inhibition. *Mol. Cancer Ther.* **7**, 809–817 (2008).
52. B. Adamson, T. M. Norman, M. Jost, M. Y. Cho, J. K. Nuñez, Y. Chen, J. E. Villalta, L. A. Gilbert, M. A. Horlbeck, M. Y. Hein, R. A. Pak, A. N. Gray, C. A. Gross, A. Dixit, O. Parnas, A. Regev, J. S. Weissman, A multiplexed single-cell CRISPR screening platform enables systematic dissection of the unfolded protein response. *Cell* **167**, 1867–1882.e21 (2016).
53. L. D. Cervia, T. Shibue, A. A. Borah, B. Gaeta, L. He, L. Leung, N. Li, S. M. Moyer, B. H. Shim, N. Dumont, A. Gonzalez, N. R. Bick, M. Kazachkova, J. M. Dempster, J. M. Krill-Burger, F. Piccioni, N. D. Udeshi, M. E. Olive, S. A. Carr, D. E. Root, J. M. McFarland, F. Vazquez, W. C. Hahn, A ubiquitination cascade regulating the integrated stress response and survival in carcinomas. *Cancer Discov.* **13**, 766–795 (2023).
54. M. Mahameed, S. Boukeileh, A. Obiedat, O. Darawshi, P. Dipta, A. Rimon, G. McLennan, R. Fassler, D. Reichmann, R. Karni, C. Preisinger, T. Wilhelm, M. Huber, B. Tirosh, Pharmacological induction of selective endoplasmic reticulum retention as a strategy for cancer therapy. *Nat. Commun.* **11**, 1304 (2020).
55. M. Fujita, R. Watanabe, N. Jaensch, M. Romanova-Michaelides, T. Satoh, M. Kato, H. Riezman, Y. Yamaguchi, Y. Maeda, T. Kinoshita, Sorting of GPI-anchored proteins into ER exit sites by p24 proteins is dependent on remodeled GPI. *J. Cell Biol.* **194**, 61–75 (2011).
56. Y.-S. Liu, X.-Y. Guo, T. Hirata, Y. Rong, D. Motooka, T. Kitajima, Y. Murakami, X.-D. Gao, S. Nakamura, T. Kinoshita, M. Fujita, N-glycan–dependent protein folding and endoplasmic reticulum retention regulate GPI-anchor processing. *J. Cell Biol.* **217**, 585–599 (2018).
57. S. Tanaka, Y. Maeda, Y. Tashima, T. Kinoshita, Inositol deacylation of glycosylphosphatidylinositol-anchored proteins is mediated by mammalian PGAP1 and yeast Bst1p. *J. Biol. Chem.* **279**, 14256–14263 (2004).
58. M. Fujita, T. Yoko-o, Y. Jigami, Inositol deacylation by Bst1p is required for the quality control of glycosylphosphatidylinositol-anchored proteins. *Mol. Biol. Cell* **17**, 834–850 (2006).
59. X. Liu, G. Hajnóczky, Altered fusion dynamics underlie unique morphological changes in mitochondria during hypoxia–reoxygenation stress. *Cell Death Differ.* **18**, 1561–1572 (2011).
60. E. Zacharioudakis, B. Agianian, V. K. MV, N. Biris, T. P. Garner, I. Rabinovich-Nikitin, A. T. Ouchida, V. Margulets, L. U. Nordstrøm, J. S. Riley, I. Dolgalev, Y. Chen, A. J. H. Wittig, R. Pekson, C. Mathew, P. Wei, A. Tsirigos, S. W. G. Tait, L. A. Kirshenbaum, R. N. Kitsis,

E. Gavathiotis, Modulating mitofusins to control mitochondrial function and signaling. *Nat. Commun.* **13**, 3775 (2022).
61. C. A. Elena-Real, A. Díaz-Quintana, K. González-Arzola, A. Velázquez-Campoy, M. Orzáez, A. López-Rivas, S. Gil-Caballero, M. Á. De la Rosa, I. Díaz-Moreno, Cytochrome c speeds up caspase cascade activation by blocking 14-3-3ε-dependent Apaf-1 inhibition. *Cell Death Dis.* **9**, 365 (2018).
62. Y. Fu, O. Sacco, E. DeBitetto, E. Kanshin, B. Ueberheide, A. Sfeir, Mitochondrial DNA breaks activate an integrated stress response to reestablish homeostasis. *Mol. Cell* **83**, 3740–3753.e9 (2023).
63. Y. Qin, W. Zhu, W. Xu, B. Zhang, S. Shi, S. Ji, J. Liu, J. Long, C. Liu, L. Liu, J. Xu, X. Yu, LSD1 sustains pancreatic cancer growth via maintaining HIF1α-dependent glycolytic process. *Cancer Lett.* **347**, 225–232 (2014).
64. K. Kosumi, Y. Baba, A. Sakamoto, T. Ishimoto, K. Harada, K. Nakamura, J. Kurashige, Y. Hiyoshi, M. Iwatsuki, S. Iwagami, Y. Sakamoto, Y. Miyamoto, N. Yoshida, E. Oki, M. Watanabe, S. Hino, M. Nakao, H. Baba, Lysine-specific demethylase-1 contributes to malignant behavior by regulation of invasive activity and metabolic shift in esophageal cancer. *Int. J. Cancer* **138**, 428–439 (2016).
65. X. Yang, R. Xia, C. Yue, W. Zhai, W. Du, Q. Yang, H. Cao, X. Chen, D. Obando, Y. Zhu, X. Chen, J.-J. Chen, J. Piganelli, P. Wipf, Y. Jiang, G. Xiao, C. Wu, J. Jiang, B. Lu, ATF4 regulates $CD4^+$ T cell immune responses through metabolic reprogramming. *Cell Rep.* **23**, 1754–1766 (2018).
66. T. Y. Li, Q. Wang, A. W. Gao, X. Li, Y. Sun, A. Mottis, M. Shong, J. Auwerx, Lysosomes mediate the mitochondrial UPR via mTORC1-dependent ATF4 phosphorylation. *Cell Discov.* **9**, 92 (2023).
67. T. Wang, X. Tian, H. B. Kim, Y. Jang, Z. Huang, C. H. Na, J. Wang, Intracellular energy controls dynamics of stress-induced ribonucleoprotein granules. *Nat. Commun.* **13**, 5584 (2022).
68. C. Giorgi, D. De Stefani, A. Bononi, R. Rizzuto, P. Pinton, Structural and functional link between the mitochondrial network and the endoplasmic reticulum. *Int. J. Biochem. Cell Biol.* **41**, 1817–1827 (2009).
69. A. Bassot, J. Chen, K. Takahashi-Yamashiro, M. C. Yap, C. S. Gibhardt, G. N. T. Le, S. Hario, Y. Nasu, J. Moore, T. Gutiérrez, L. Mina, H. Mast, A. Moses, R. Bhat, K. Ballanyi, H. Lemieux, R. Sitia, E. Zito, I. Bogeski, R. E. Campbell, T. Simmen, The endoplasmic reticulum kinase PERK interacts with the oxidoreductase ERO1 to metabolically adapt mitochondria. *Cell Rep.* **42**, 111899 (2022).
70. R. Bravo-Sagua, C. López-Crisosto, V. Parra, M. Rodriguez-Peña, B. A. Rothermel, A. F. G. Quest, S. Lavandero, mTORC1 inhibitor rapamycin and ER stressor tunicamycin induce differential patterns of ER-mitochondria coupling. *Sci. Rep.* **6**, 36394 (2016).
71. R. Bravo-Sagua, V. Parra, C. Ortiz-Sandoval, M. Navarro-Marquez, A. E. Rodríguez, N. Diaz-Valdivia, C. Sanhueza, C. Lopez-Crisosto, N. Tahbaz, B. A. Rothermel, J. A. Hill, M. Cifuentes, T. Simmen, A. F. G. Quest, S. Lavandero, Caveolin-1 impairs PKA-DRP1-mediated remodelling of ER–mitochondria communication during the early phase of ER stress. *Cell Death Differ.* **26**, 1195–1212 (2019).
72. J. R. Hom, J. S. Gewandter, L. Michael, S. Sheu, Y. Yoon, Thapsigargin induces biphasic fragmentation of mitochondria through calcium-mediated mitochondrial fission and apoptosis. *J. Cell. Physiol.* **212**, 498–508 (2007).
73. X. Hu, B. Guo, T. Sun, W. Wang, Inhibition of glycolysis represses the growth and alleviates the endoplasmic reticulum stress of breast cancer cells by regulating TMTC3. *Open Med.* **18**, (2023).
74. R. M. Graham, F. Hernandez, N. Puerta, G. De Angulo, K. A. Webster, S. Vanni, Resveratrol augments ER stress and the cytotoxic effects of glycolytic inhibition in neuroblastoma by downregulating Akt in a mechanism independent of SIRT1. *Exp. Mol. Med.* **48**, e210–e210 (2016).
75. O. M. de Brito, L. Scorrano, Mitofusin 2 tethers endoplasmic reticulum to mitochondria. *Nature* **456**, 605–610 (2008).
76. R. G. Abrisch, S. C. Gumbin, B. T. Wisniewski, L. L. Lackner, G. K. Voeltz, Fission and fusion machineries converge at ER contact sites to regulate mitochondrial morphology. *J. Cell Biol.* **219**, (2020).
77. K. I. Pishas, C. D. Drenberg, C. Taslim, E. R. Theisen, K. M. Johnson, R. S. Saund, I. L. Pop, B. D. Crompton, E. R. Lawlor, F. Tirode, J. Mora, O. Delattre, M. C. Beckerle, D. F. Callen, S. Sharma, S. L. Lessnick, Therapeutic targeting of KDM1A/LSD1 in Ewing Sarcoma with SP-2509 engages the endoplasmic reticulum stress response. *Mol. Cancer Ther.* **17**, 1902–1916 (2018).
78. H. Wang, Z. Song, E. Xie, J. Chen, B. Tang, F. Wang, J. Min, Targeting the LSD1-G9a-ER stress pathway as a novel therapeutic strategy for esophageal squamous cell carcinoma. *Research* **2022**, 9814652 (2022).
79. G. R. Sareddy, S. Viswanadhapalli, P. Surapaneni, T. Suzuki, A. Brenner, R. K. Vadlamudi, Novel KDM1A inhibitors induce differentiation and apoptosis of glioma stem cells via unfolded protein response pathway. *Oncogene* **36**, 2423–2434 (2017).
80. J. J. Rodvold, S. Xian, J. Nussbacher, B. Tsui, T. Cameron Waller, S. C. Searles, A. Lew, P. Jiang, I. Babic, N. Nomura, J. H. Lin, S. Kesari, H. Carter, M. Zanetti, IRE1α and IGF signaling predict resistance to an endoplasmic reticulum stress-inducing drug in glioblastoma cells. *Sci. Rep.* **10**, 8348 (2020).
81. D. Y. A. Dadey, V. Kapoor, A. Khudanyan, D. Thotala, D. E. Hallahan, PERK regulates glioblastoma sensitivity to er stress although promoting radiation resistance. *Mol. Cancer Res.* **16**, 1447–1453 (2018).
82. C. E. Griguer, C. R. Oliva, G. Y. Gillespie, Glucose metabolism heterogeneity in human and mouse malignant glioma cell lines. *J. Neurooncol* **74**, 123–133 (2005).
83. J. Lebeau, J. M. Saunders, V. W. R. Moraes, A. Madhavan, N. Madrazo, M. C. Anthony, R. L. Wiseman, The PERK arm of the unfolded protein response regulates mitochondrial morphology during acute endoplasmic reticulum stress. *Cell Rep.* **22**, 2827–2836 (2018).
84. T. Verfaillie, N. Rubio, A. D. Garg, G. Bultynck, R. Rizzuto, J.-P. Decuypere, J. Piette, C. Linehan, S. Gupta, A. Samali, P. Agostinis, PERK is required at the ER-mitochondrial contact sites to convey apoptosis after ROS-based ER stress. *Cell Death Differ.* **19**, 1880–1891 (2012).
85. E. Balsa, M. S. Soustek, A. Thomas, S. Cogliati, C. García-Poyatos, E. Martín-García, M. Jedrychowski, S. P. Gygi, J. A. Enriquez, P. Puigserver, ER and nutrient stress promote assembly of respiratory chain supercomplexes through the PERK-eIF2α axis. *Mol. Cell* **74**, 877–890.e6 (2019).
86. G. Ong, R. Ragetli, K. Mnich, B. W. Doble, W. Kammouni, S. E. Logue, IRE1 signaling increases PERK expression during chronic ER stress. *Cell Death Dis.* **15**, 276 (2024).
87. Y. Murakami, H. Tawamie, Y. Maeda, C. Büttner, R. Buchert, F. Radwan, S. Schaffer, H. Sticht, M. Aigner, A. Reis, T. Kinoshita, R. A. Jamra, Null mutation in PGAP1 impairing Gpi-anchor maturation in patients with intellectual disability and encephalopathy. *PLOS Genet.* **10**, e1004320 (2014).
88. P. Kim, M. R. Scott, J. H. Meador-Woodruff, Abnormal ER quality control of neural GPI-anchored proteins via dysfunction in ER export processing in the frontal cortex of elderly subjects with schizophrenia. *Transl. Psychiatry* **9**, 6 (2019).
89. M. Kettwig, O. Elpeleg, E. Wegener, S. Dreha-Kulaczewski, M. Henneke, J. Gärtner, P. Huppke, Compound heterozygous variants in PGAP1 causing severe psychomotor retardation, brain atrophy, recurrent apneas and delayed myelination: A case report and literature review. *BMC Neurol.* **16**, 74 (2016).
90. X.-X. Zhang, B. Ni, Q. Li, L.-P. Hu, S.-H. Jiang, R.-K. Li, G.-A. Tian, L.-L. Zhu, J. Li, X.-L. Zhang, Y.-L. Zhang, X.-M. Yang, Q. Yang, Y.-H. Wang, C.-C. Zhu, Z.-G. Zhang, GPAA1 promotes gastric cancer progression via upregulation of GPI-anchored protein and enhancement of ERBB signalling pathway. *J. Exp. Clin. Cancer Res.* **38**, 214 (2019).
91. M. van Veen, E. Matas-Rico, K. van de Wetering, D. Leyton-Puig, K. M. Kedziora, V. De Lorenzi, Y. Stijf-Bultsma, B. van den Broek, K. Jalink, N. Sidenius, A. Perrakis, W. H. Moolenaar, Negative regulation of urokinase receptor activity by a GPI-specific phospholipase C in breast cancer cells. *eLife* **6**, e23649 (2017).
92. G. Wu, Z. Guo, A. Chatterjee, X. Huang, E. Rubin, F. Wu, E. Mambo, X. Chang, M. Osada, M. Sook Kim, C. Moon, J. A. Califano, E. A. Ratovitski, S. M. Gollin, S. Sukumar, D. Sidransky, B. Trink, Overexpression of Glycosylphosphatidylinositol (GPI) transamidase subunits phosphatidylinositol glycan Class T and/or GPI anchor attachment 1 induces tumorigenesis and contributes to invasion in human breast cancer. *Cancer Res.* **66**, 9829–9836 (2006).
93. J. Hong, T. Li, Y. Chao, Y. Xu, Z. Zhu, Z. Zhou, W. Gu, Q. Qu, D. Li, Molecular basis of the inositol deacylase PGAP1 involved in quality control of GPI-AP biogenesis. *Nat. Commun.* **15**, 8 (2024).
94. S. Alejo, B. E. Palacios, P. P. Venkata, Y. He, W. Li, J. D. Johnson, Y. Chen, S. Jayamohan, U. P. Pratap, K. Clarke, Y. Zou, Y. Lv, K. Weldon, S. Viswanadhapalli, Z. Lai, Z. Ye, Y. Chen, A. R. Gilbert, T. Suzuki, R. R. Tekmal, W. Zhao, S. Zheng, R. K. Vadlamudi, A. J. Brenner, G. R. Sareddy, Lysine-specific histone demethylase 1A (KDM1A/LSD1) inhibition attenuates DNA double-strand break repair and augments the efficacy of temozolomide in glioblastoma. *Neuro Oncol.* **25**, 1249–1261 (2023).
95. G. Xiang, S. Wang, L. Chen, M. Song, X. Song, H. Wang, P. Zhou, X. Ma, J. Yu, UBR5 targets tumor suppressor CDC73 proteolytically to promote aggressive breast cancer. *Cell Death Dis.* **13**, 451 (2022).
96. Q. Liang, C. Tang, M. Tang, Q. Zhang, Y. Gao, Z. Ge, TRIM47 is up-regulated in colorectal cancer, promoting ubiquitination and degradation of SMAD4. *J. Exp. Clin. Cancer Res.* **38**, 159 (2019).
97. F. Meitinger, M. Ohta, K.-Y. Lee, S. Watanabe, R. L. Davis, J. V. Anzola, R. Kabeche, D. A. Jenkins, A. K. Shiau, A. Desai, K. Oegema, TRIM37 controls cancer-specific vulnerability to PLK4 inhibition. *Nature* **585**, 440–446 (2020).
98. K. Tanaka, T. Sasayama, Y. Irino, K. Takata, H. Nagashima, N. Satoh, K. Kyotani, T. Mizowaki, T. Imahori, Y. Ejima, K. Masui, B. Gini, H. Yang, K. Hosoda, R. Sasaki, P. S. Mischel, E. Kohmura, Compensatory glutamine metabolism promotes glioblastoma resistance to mTOR inhibitor treatment. *J. Clin. Investig.* **125**, 1591–1602 (2015).
99. D. Wang, A. Berglund, R. S. Kenchappa, P. A. Forsyth, J. J. Mulé, A. B. Etame, BIRC3 is a novel driver of therapeutic resistance in Glioblastoma. *Sci. Rep.* **6**, 21710 (2016).
100. E. N. Perrault, J. M. Shireman, E. S. Ali, P. Lin, I. Preddy, C. Park, S. Budhiraja, S. Baisiwala, K. Dixit, C. D. James, D. H. Heiland, I. Ben-Sahra, S. Pott, A. Basu, J. Miska, A. U. Ahmed,

Ribonucleotide reductase regulatory subunit M2 drives glioblastoma TMZ resistance through modulation of dNTP production. *Sci. Adv.* **9**, eade7236 (2023).
101. J. J. Harding, M. Telli, P. Munster, M. H. Voss, J. R. Infante, A. DeMichele, M. Dunphy, M. H. Le, C. Molineaux, K. Orford, F. Parlati, S. H. Whiting, M. K. Bennett, N. M. Tannir, F. Meric-Bernstam, A phase I dose-escalation and expansion study of telaglenastat in patients with advanced or metastatic solid tumors. *Clin. Cancer Res.* **27**, 4994–5003 (2021).
102. B. Noce, E. Di Bello, R. Fioravanti, A. Mai, LSD1 inhibitors for cancer treatment: Focus on multi-target agents and compounds in clinical trials. *Front. Pharmacol.* **14**, (2023).
103. L. M. Stitzlein, A. Gangadharan, L. M. Walsh, D. Nam, A. B. Espejo, M. M. Singh, K. H. Patel, Y. Lu, X. Su, R. Ezhilarasan, J. Gumin, S. Singh, E. Sulman, F. F. Lang, J. Chandra, Comparison of pharmacological inhibitors of lysine-specific demethylase 1 in glioblastoma stem cells reveals inhibitor-specific efficacy profiles. *Front. Neurol.* **14**, 1112207 (2023).
104. K. Shinjo, T. Umehara, H. Niwa, S. Sato, K. Katsushima, S. Sato, X. Wang, Y. Murofushi, M. M. Suzuki, H. Koyama, Y. Kondo, Novel pharmacologic inhibition of lysine-specific demethylase 1 as a potential therapeutic for glioblastoma. *Cancer Gene Ther.* **31**, 1884–1894 (2024).
105. B. Ortensi, D. Osti, S. Pellegatta, F. Pisati, P. Brescia, L. Fornasari, D. Levi, P. Gaetani, P. Colombo, A. Ferri, S. Nicolis, G. Finocchiaro, G. Pelicci, Rai is a new regulator of neural progenitor migration and glioblastoma invasion. *Stem Cells* **30**, 817–832 (2012).
106. C. Stringer, T. Wang, M. Michaelos, M. Pachitariu, Cellpose: A generalist algorithm for cellular segmentation. *Nat. Methods* **18**, 100–106 (2021).
107. J. Lam, P. Katti, M. Biete, M. Mungai, S. AshShareef, K. Neikirk, E. Garza Lopez, Z. Vue, T. A. Christensen, H. K. Beasley, T. A. Rodman, S. A. Murray, J. L. Salisbury, B. Glancy, J. Shao, R. O. Pereira, E. D. Abel, A. Hinton, *A universal approach to analyzing transmission electron microscopy with ImageJ*, *Cells* **10**, 2177 (2021).
108. B. Talone, A. Bresci, F. Manetti, F. Vernuccio, A. De la Cadena, C. Ceconello, M. L. Schiavone, S. Mantero, C. Menale, R. Vanna, G. Cerullo, C. Sobacchi, D. Polli, Label-free multimodal nonlinear optical microscopy reveals features of bone composition in pathophysiological conditions. *Front. Bioeng. Biotechnol.* **10**, (2022).
109. Y. Wen, H. N. Xu, L. Privette Vinnedge, M. Feng, L. Z. Li, Optical redox imaging detects the effects of DEK oncogene knockdown on the redox state of MDA-MB-231 breast cancer cells. *Mol. Imaging Biol.* **21**, 410–416 (2019).
110. F. Vernuccio, R. Vanna, C. Ceconello, A. Bresci, F. Manetti, S. Sorrentino, S. Ghislanzoni, F. Lambertucci, O. Motiño, I. Martins, G. Kroemer, I. Bongarzone, G. Cerullo, D. Polli, Full-spectrum CARS microscopy of cells and tissues with ultrashort white-light continuum pulses. *J. Phys. Chem. B* **127**, 4733–4745 (2023).
111. S. R. Alam, H. Wallrabe, Z. Svindrych, A. K. Chaudhary, K. G. Christopher, D. Chandra, A. Periasamy, Investigation of mitochondrial metabolic response to doxorubicin in prostate cancer cells: An NADH, FAD and tryptophan FLIM assay. *Sci. Rep.* **7**, 10451 (2017).
112. J.-C. Yen, F.-J. Chang, S. Chang, A new criterion for automatic multilevel thresholding. *IEEE Trans. Image Process.* **4**, 370–378 (1995).
113. J. Cox, M. Mann, MaxQuant enables high peptide identification rates, individualized p.p.b.-range mass accuracies and proteome-wide protein quantification. *Nat. Biotechnol.* **26**, 1367–1372 (2008).
114. J. Cox, M. Y. Hein, C. A. Luber, I. Paron, N. Nagaraj, M. Mann, Accurate proteome-wide label-free quantification by delayed normalization and maximal peptide ratio extraction, Termed MaxLFQ. *Mol. Cell. Proteomics* **13**, 2513–2526 (2014).
115. B. Li, C. N. Dewey, RSEM: Accurate transcript quantification from RNA-seq data with or without a reference genome. *BMC Bioinformatics* **12**, 323 (2011).
116. E. Lazzarini, D. A. Silvestris, G. Benvenuto, D. Osti, L. Fattore, R. Paterra, G. Finocchiaro, P. Malatesta, A. Daga, A. L. Gallotti, R. Galli, G. Pelicci, A. Tesei, M. Bedeschi, R. Pallini, L. Pasqualini, C. Romualdi, A. Gallo, L. Ricci-Vitiani, S. Indraccolo, Genome-wide profiling of patient-derived glioblastoma stem-like cells reveals recurrent genetic and transcriptomic signatures associated with brain tumors. *J. Neurooncol.* **163**, 47–59 (2023).
117. E. Cerami, J. Gao, U. Dogrusoz, B. E. Gross, S. O. Sumer, B. A. Aksoy, A. Jacobsen, C. J. Byrne, M. L. Heuer, E. Larsson, Y. Antipin, B. Reva, A. P. Goldberg, C. Sander, N. Schultz, The cBio cancer genomics portal: An open platform for exploring multidimensional cancer genomics data. *Cancer Discov.* **2**, 401–404 (2012).
118. Z. Tang, B. Kang, C. Li, T. Chen, Z. Zhang, GEPIA2: An enhanced web server for large-scale expression profiling and interactive analysis. *Nucleic Acids Res.* **47**, W556–W560 (2019).
119. M. Kanehisa, KEGG: Kyoto Encyclopedia of Genes and Genomes. *Nucleic Acids Res.* **28**, 27–30 (2000).
120. J. A. Vizcaíno, E. W. Deutsch, R. Wang, A. Csordas, F. Reisinger, D. Ríos, J. A. Dianes, Z. Sun, T. Farrah, N. Bandeira, P.-A. Binz, I. Xenarios, M. Eisenacher, G. Mayer, L. Gatto, A. Campos, R. J. Chalkley, H.-J. Kraus, J. P. Albar, S. Martinez-Bartolomé, R. Apweiler, G. S. Omenn, L. Martens, A. R. Jones, H. Hermjakob, ProteomeXchange provides globally coordinated proteomics data submission and dissemination. *Nat. Biotechnol.* **32**, 223–226 (2014).

Acknowledgments: We thank L. Lanfrancone for metabolic library provision, technical assistance, and useful discussion and N. Mitro for intellectual discussion. We thank M. Marenda for support with image analysis, G. Cugliari for statistical analysis support, G. Giardina for experimental assistance in drug testing readouts, and B. Pollo and M. Patanè for the help in tissue sampling preparation and analysis. We thank G. G. Schiattarella for the contribution in the design of the UPRE-XBP1 vector and G. Peccati for support in the analysis of zebrafish xenografts. We acknowledge help from Flow Cytometry, Genomics, Cell Culture, and Molecular and Digital Pathology Units from EIO. **Funding:** This work was supported by grant from the Italian Association for Cancer Research (AIRC, investigator grant ID: 27014 to G.P.) and partially by the Italian Ministry of Health with Ricerca Corrente and 5 × 1000 funds (to EIO IRCCS); funding from MDC, Helmholtz (VH-NG-1153), ERC (StG:714922 and PoC:101069235), Deutsche Krebshilfe (7011508), and DFG (GA3203/3–1) (to G.G.); grants from the Italian Association for Cancer Research (AIRC, investigator grant ID: 24415) and European Research Council ERC-CoG2020 101002280 (to S.S.); grant from the Italian Association for Cancer Research (AIRC, investigator grant ID: 22080 to A.G.); and funding from Research to Care by Sanofy Genzyme (to E.M.) and NextGeneration EU PRIN 2022 Prot. 20229CJ27R and NextGeneration EU PRIN 2022 PNRR Prot. P2022AFS8P (to D.C.). G.M. was a PhD student at the European School of Molecular Medicine (SEMM) and is supported by the AIRC Fellowship "Mario e Valeria Rindi". E.Z. and A.M. are PhD students at the European School of Molecular Medicine (SEMM). B.C. was supported by Fondazione Umberto Veronesi fellowship in collaboration with "Il dono di Rossana". S.F. was supported by Fondazione IEO-Monzino fellowship and Brainy grant. **Author contributions:** Conceptualization: G.M., D.O., E.Z., B.C., S.F., G.V.B., M.-C.R., V.G., G.G., and G.P. Methodology: G.M., D.O., B.C., S.R., C.S., E.M., F.R., F.M., G.V.B., M.-C.R., V.G., F.A., S.G., G.G., and G.P. Investigation: G.M., D.O., E.Z., E.M., B.C., S.F., A.M., C.R., D.M., S.R., C.S., C.P., F.M., D.P., T.B., G.V.B., M.-C.R., M.J.S., and R.N. Validation: G.M., D.O., E.Z., B.C., S.F., A.M., D.M., S.R., C.S., G.G., E.M., A.G., G.V.B., M.-C.R., M.J.S., and G.P. Visualization: G.M., D.O., M.-C.R., S.G., E.Z., and G.P. Formal analysis: G.M., D.O., B.C., S.F., D.M., S.R., C.S., F.M., G.V.B., M.-C.R., F.F., D.C., F.A., S.G., A.G., V.G., M.J.S., D.A.S., and R.N. Software: C.S., F.A., and S.G. Data curation: G.M., D.O., B.C., S.G., F.F., and D.C. Project administration: G.G. and G.P. Supervision: E.M., S.S., D.P., D.C., B.C., G.G., T.B., and G.P. Resources: S.R., F.R., S.S., A.G., G.V.B., M.-C.R., D.C., B.C., G.G., and G.P. Writing—original draft: G.M., D.O., G.V.B., S.G., and G.P. Writing—review and editing: G.M., D.O., B.C., S.F., M.-C.R., A.G., G.G., T.B., and G.P. Funding acquisition: G.P. **Competing interests:** The authors declare that they have no competing interests. **Data and materials availability:** All data needed to evaluate the conclusions in the paper are present in the paper and/or the Supplementary Materials. The MS proteomics data have been deposited to the ProteomeXchange Consortium (*120*) via the PRIDE partner repository with the dataset identifier PXD053770. This accession number is listed in the key resources table. The RNA-seq data generated in this study are not publicly available because of restrictions related to patients' privacy. RNA-seq data, along with further information and requests for resources and reagents, can be provided by Giuliana Pelicci pending scientific review and a completed material transfer agreement. Requests should be submitted to G.P. (giuliana.pelicci@ieo.it).

Submitted 20 September 2024
Accepted 17 April 2025
Published 23 May 2025
10.1126/sciadv.adt2724